Martin Wilkening*, Andre Düvel, Florian Preishuber-Pflügl, Klebson da Silva, Stefan Breuer, Vladimir Šepelák* and Paul Heitjans*

Structure and ion dynamics of mechanosynthesized oxides and fluorides

Access to nanocrystalline ceramics via high-energy ball-milling – a short review

DOI 10.1515/zkri-2016-1963
Received May 30, 2016; accepted August 16, 2016; published online September 22, 2016

Abstract: In many cases, limitations in conventional synthesis routes hamper the accessibility to materials with properties that have been predicted by theory. For instance, metastable compounds with local non-equilibrium structures can hardly be accessed by solid-state preparation techniques often requiring high synthesis temperatures. Also other ways of preparation lead to the thermodynamically stable rather than metastable products. Fortunately, such hurdles can be overcome by mechanochemical synthesis. Mechanical treatment of two or three starting materials in high-energy ball mills enables the synthesis of not only new, metastable compounds but also of nanocrystalline materials with unusual or enhanced properties such as ion transport. In this short review we report about local structures and ion transport of oxides and fluorides mechanochemically prepared by high-energy ball-milling.

Keywords: ball milling; conductivity; nanocrystalline ceramics; NMR; non-equilibrium phases.

***Corresponding authors: Martin Wilkening,** Institute for Chemistry and Technology of Materials (member of NAWI Graz), Graz University of Technology, Stremayrgasse 9, A-8010 Graz, Austria; and Institute of Physical Chemistry and Electrochemistry, Leibniz Universität Hannover, Callinstraße 3-3a, D-30167 Hannover, Germany, E-mail: wilkening@tugraz.at; **Vladimir Šepelák,** Institute of Nanotechnology, Karlsruhe Institute of Technology, Hermann-von-Helmholtz-Platz 1, D-76344 Eggenstein-Leopoldshafen, Germany, E-mail: vladimir.sepelak@kit.edu; and **Paul Heitjans,** Institute of Physical Chemistry and Electrochemistry, Zentrum für Festkörperchemie und Neue Materialien (ZFM), Leibniz Universität Hannover, Callinstraße 3-3a, D-30167 Hannover, Germany, E-mail: heitjans@pci.uni-hannover.de
Andre Düvel: Institute of Physical Chemistry and Electrochemistry, Zentrum für Festkörperchemie und Neue Materialien (ZFM), Leibniz Universität Hannover, Callinstraße 3-3a, D-30167 Hannover, Germany
Florian Preishuber-Pflügl and Stefan Breuer: Institute for Chemistry and Technology of Materials (member of NAWI Graz), Graz University of Technology, Stremayrgasse 9, A-8010 Graz, Austria
Klebson da Silva: Institute of Physical and Theoretical Chemistry, Technische Universität Braunschweig, Hans-Sommer-Str. 10, D-38106 Braunschweig, Germany; Institute of Physical Chemistry and Electrochemistry, Leibniz Universität Hannover, Callinstr. 3-3a, D-30167 Hannover, Germany; Department of Physics of Materials, State University of Maringá, Av. Colombo 5790, 87020900 Maringá, Brazil; and Institute of Nanotechnology, Karlsruhe Institute of Technology, Hermann-von-Helmholtz-Platz 1, D-76344 Eggenstein-Leopoldshafen, Germany

Introduction and motivation

Materials science involves the discovery and development of new materials. Besides structural investigations it includes the study of the various chemical and physical properties. Making available compounds with yet inaccessible features takes a front-seat role in materials science. Mechanochemistry [1, 2], that is, high-energy ball milling, offers the possibility to prepare ceramic materials being characterized by non-equilibrium local structures [3, 4]. While conventional routes often yield thermodynamically stable compounds, mechanosynthesis is able to provide direct access to metastable, novel phases through a facile and efficient one-step approach. Simultaneously, the materials obtained are composed of nm-sized crystallites [5–9] usually assembled in larger clusters. Therefore, they may benefit from unusual functional properties markedly different from those of their bulk-sized counterparts [4]. Enabling access to such functional materials provides a major source of motivation for their mechanically induced formation [3].

For the successful preparation of such non-equilibrium, nanocrystalline materials high temperatures are to be avoided, but, at the same time, the conditions under which they are formed need to be present. Mechanochemistry fulfills these, at first glance, contradictory requirements. Although carried out at ambient conditions, during the irregular and fast movement of the milling balls interacting with the vial and the reactants, spots of high pressure and temperature are generated for an extremely short duration. These processes bring along the conditions necessary

to form non-equilibrium structures that are immediately frozen in. Hence, the product obtained is characterized by the preserved properties belonging to the corresponding high-temperature or high-pressure phases, respectively.

High-energy ball milling is well suited to prepare inorganic ceramic materials such as sulfides, oxides and fluorides [10–21]. The variation of the milling conditions, that is, milling time, rotation speed, vial sets, number and kind of balls (size, material), offers a rich playground of possibilities to find the best route to prepare yet unknown materials. For instance, mechanosynthesis if carried out for sufficiently long milling times is able to close miscibility gaps, i.e. it yields solid solutions that are otherwise impossible to prepare [10, 14]. In the following, after a brief introduction into mechanochemical reactions, we present case studies on mechanosynthesized oxides and fluorides prepared and characterized in our labs during the last years. In some cases metastable materials with unusual local structures are formed that benefit from non-equilibrium cation distributions, spin arrangements or distorted polyhedra geometries. In many cases, metastable local structures and defects introduced during mechanical treatment lead to enhanced ion dynamics.

Mechanochemistry

Every chemical reaction requires a certain amount of energy to proceed. For most reactions, this energy is provided by heat, light or by differing electrochemical potentials. In a mechanochemical reaction, the energy is provided by mechanical activation. An overview is given by some very comprehensive reviews that were published in the literature lately. In terms of solid state chemistry, mechanochemical reactions mainly show two characteristic aspects. The mechanical treatment of solids leads to a reduction in size of the particles and can, under certain conditions, initiate a chemical reaction and induce the conversion to a material with different properties. The typical degradation mechanisms and morphological changes that occur during the milling process are abrasion, erosion and (crystallite) fracture. The shear and friction forces between the milling tools and the particles lead to abrasion and fracture of the grains. The continuous reduction in size yields an increased surface. Moreover, many of the defects, such as point defects and screw or edge dislocations, are formed due to the impact of the grinding media on the crystallites. Both processes may have a significant influence on the properties of the material treated such as, e.g. the diffusion of ionic charge carriers. For mechanical treatment, many techniques are available that are described elsewhere in literature [2, 22]. The materials that are presented in this study were prepared either by high-energy planetary mills or by shaker mills.

The active parts of a planetary ball mill consist of a rotating disk carrying two beakers that rotate in opposite direction to the disk, as it is shown in Figure 1. The milling tools are made of materials like hardened, corrosion resistant steel, zirconium dioxide or tungsten carbide that resist the harsh synthesis conditions. The use of such material minimizes the degradation of the tools and possible contamination of the synthesized compounds. During the milling process, shear and friction forces grind and erode the particles when the balls move along the walls due to centrifugal forces. The contra-rotating beakers and supporting disk further lead to an acceleration of the milling balls at a certain point of the rotation so that they move across the beaker and impact on the opposite side, see Figure 1. At this point, the high impact forces of the balls can further crush the particles or induce deformations of the crystal which creates structural defects. Beside the size reduction and structural modifications, mechanical treatment can trigger chemical reactions. The energy required for the initialization of such reactions originates from the evolution of heat and pressure at the contact spots of the particles. First theories from Bowden, Tabor and Yoffe predict temperatures of about 1000 K upon friction at surfaces of ca. 1 μm^2 for 10^{-3} to 10^{-4} s [23–25]. Other theories like the Magma-Plasma Model proposes even higher temperatures of up to 10,000 K [26]. A detailed summary of various models and theories describing the effects in mechanochemistry can be found in the book of P. Baláž [27]. The common sense in most of the theories is a very localized evolution of heat that initiates the chemical reaction. As mentioned above, these conditions enable the direct synthesis of new crystalline and amorphous compounds that are not accessible by

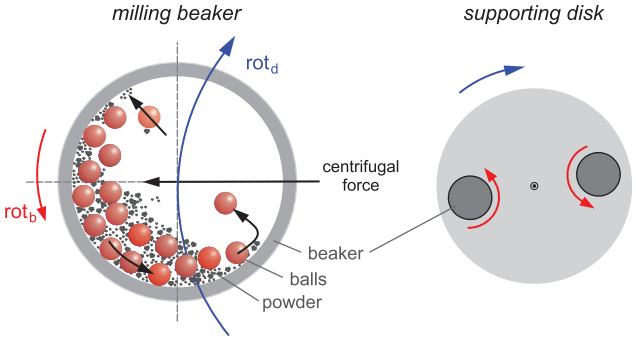

Fig. 1: Illustration of the milling tools and the principle of operation of a planetary mill. The colored arrows indicate the counter-rotation of the supporting disk (rot$_d$) and the milling beakers (rot$_b$).

conventional methods. For example, this holds for amorphous phases that would crystallize upon heating, and metastable, or non-equilibrium phases that show crystal structures which differ from the thermodynamically more stable modifications can be prepared.

If the milling procedure is stopped by switching off the mill the synthesis process is immediately interrupted; hence, the evolution of the product can directly be followed as a function of milling time. By doing so, formation mechanisms can be studied if local and macroscopic structures are studied by, e.g. diffraction techniques or (solid-state) nuclear magnetic resonance carried out under high-resolution conditions.

Nanocrystalline ceramics

Nanocrystalline compounds can be defined as materials of which a single unit, i.e. a single crystallite, is sized between 1 and 100 nm. In general, at least one dimension of the individual particles should be less than 100 nm. Their small dimensions often account for properties that are different to those of the commonly used, larger-sized counterparts, that is, their microcrystalline analogs. Although the overall chemical composition of micro- and nanocrystalline materials is the same, local compositions in nanocrystalline ceramics may vary from those of their coarse-grained relatives [5, 8].

In terms of crystalline solids or ion conductors, this difference can have important consequences on localized and through-going, i.e. macroscopic ion transport [5, 7, 8, 28–31]. In general, boundaries of grains or crystallites diverge in their behavior from bulk material. Both the short-range and long-range order is different as the boundary atoms are facing distinct bonding environments. As nanocrystalline solids possess much larger surface areas the increased area of grain boundaries or interfacial regions can result in much different properties [5, 28]. The relationship between grain size and the percentage of atoms, which are located in such boundaries is described in Figure 2a. The solid line assumes a boundary layer thickness of 1 nm and the dotted line a thickness of 0.5 nm. Figure 2b illustrates such nanocrystallites by highlighting the surface located atoms as well as those residing in the surface-influenced volume.

Nanomaterials have found numerous applications in solid-state ionics, particularly in energy-related research of batteries and solid electrolytes. The short diffusion length scales, for example, have opened new possibilities for materials with generally poor bulk properties. As an example, $LiFePO_4$, which is common to be the active material in cathodes of lithium-ion batteries, is a poor ion conductor that exhibits low Li^+ insertion rates if used as a coarse grained compound but shows good rates as a defect-rich nanocrystalline material [32]. Considering transport of small ions such as Li and F many other materials show similar behavior; hence, nano-sizing became a major trend in energy-related materials chemistry and materials engineering [9, 33–37]. Nanocrystalline CaF_2 is the first ceramic material where an increase in F ion conductivity and jump rate by several orders of magnitude as compared to coarse grained or single crystalline CaF_2 was found [38–40], see also [5, 41]. In particular, ion transport properties can be drastically influenced by taking advantage of so-called non-trivial size effects, i.e. by making use of (overlapping) space charge zones affecting the electrochemical and dynamic properties of the ions in *or near* such regions [42–46].

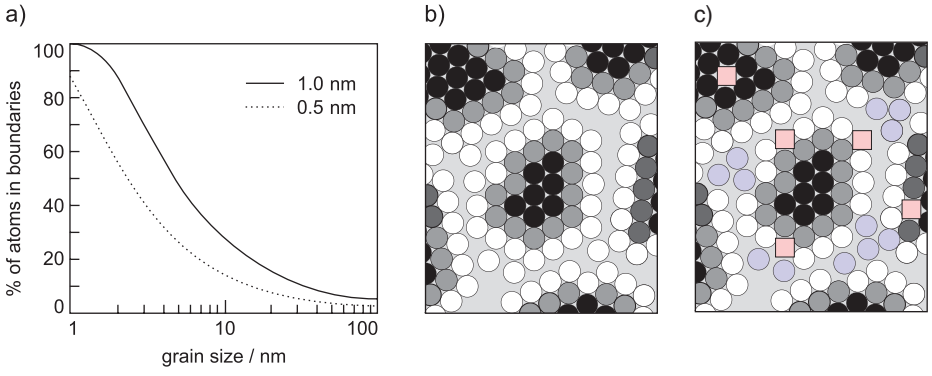

Fig. 2: Relationship between average grain (crystallite) size and the percentage of atoms located in grain boundaries, interfacial regions. Adapted from reference [28]. (b) and (c) Illustration of a single-phase nanocrystalline solid. Black circles denote atoms or ions in the crystalline grain. White and gray circles represent those on the surface and in the surface-influenced volume. In (c) defects are introduced in both the interfacial regions and the bulk. Circles in blue represent amorphous regions.

Mechanosynthesized ceramics

Complex fluorides

Earth-alkaline mixed, cubic $(Ba,Ca)F_2$

CaF_2, SrF_2 and BaF_2 were the subject of many studies devoted to understand F anion dynamics in binary fluorides. F anions either use interstitial sites or vacancies to diffuse in the cubic structure [47]. Mechanical treatment of the fluorides causes the ionic conductivity to increase by several orders of magnitude [15, 16]. It has been shown that mixing of CaF_2 and SrF_2 leads to thermodynamically stable solid solutions; the same holds for $(Ba,Sr)F_2$ (see Figure 3a). If the difference in radii of the cations is, however, too large the formation of a ternary compound crystallizing with a different crystal structure is expected. As an example, BaF_2 when mixed with equimolar amounts of LiF leads to the formation of $BaLiF_3$ crystallizing with inverse perovskite structure [48]. Of course, this estimation depends on the molar ratio of the reactants. For Ca^{2+} and Ba^{2+}, when mixed in equimolar ratios, the difference in cation radii does not favor the formation of a non-cubic phase. Instead, heavy ball-milling using planetary mills forces the two fluorides to form a metastable solid solution, $Ba_{1-x}Ca_xF_2$, while preserving the initial cubic symmetry (Figure 4) [16].

^{19}F magic angle spinning (MAS) nuclear magnetic resonance spectroscopy (NMR) is able to uncover the local F environments formed in $(Ca,Sr)F_2$, $(Ba,Sr)F_2$ and $(Ba,Ca)F_2$ (Figure 3). The F anions are coordinated by a different number of Ca and Ba ions reflected by distinct isotropic chemical shift values. For $Ba_{0.5}Ca_{0.5}F_2$ the majority of the F anions are located in environments like $[Ba]_3[Ca]$, $[Ba]_2[Ca]_2$ or $[Ba][Ca]_3$. The mismatch in size causes strain which has direct effect on F anion dynamics in the mixed compound. Local stress is maximized at compositions around $x = 0.5$; thus long-range ion transport in $Ba_{1-x}Ca_xF_2$ is expected to be mostly influenced at this composition. Indeed, the ionic conductivity, read out from the frequency independent plateaus of the isotherms shown in Figure 5,

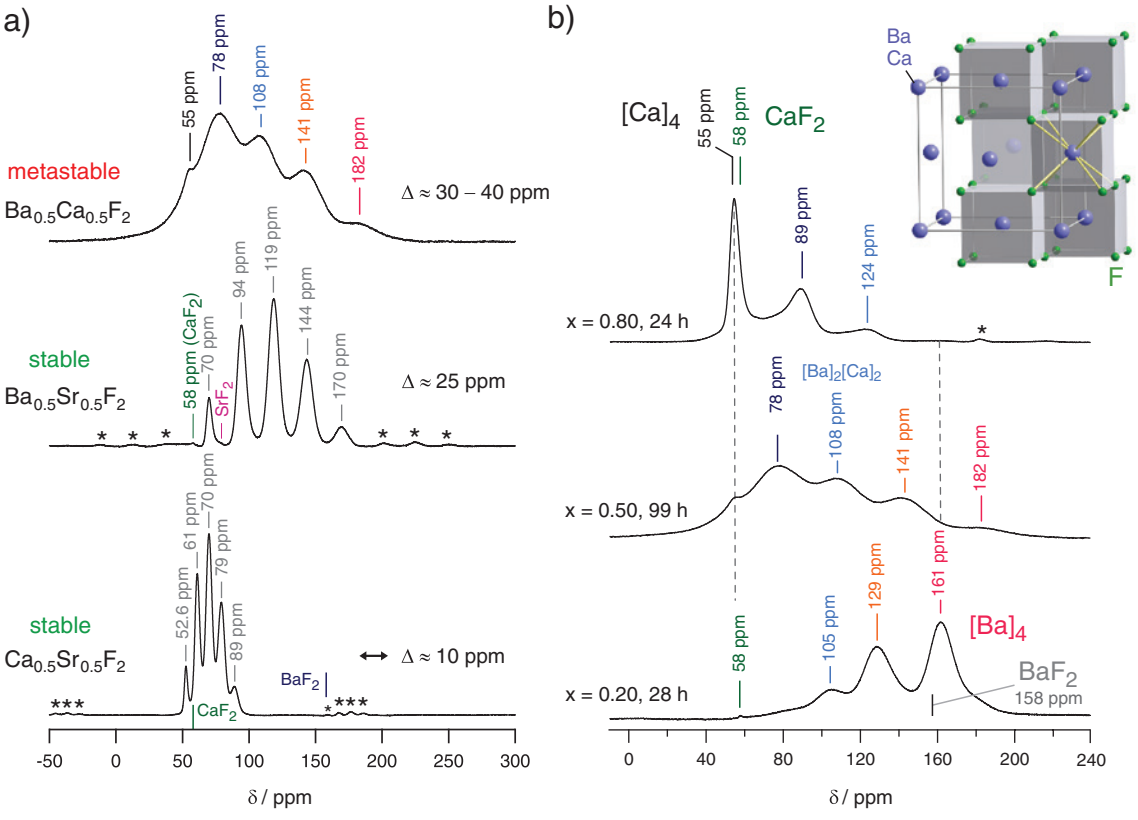

Fig. 3: Mixing of BaF_2 with CaF_2 via high-energy ball-milling: the mismatch in size forces the fluorides to arrange in a cubic structure $Ba_{1-x}Ca_xF_2$ yielding a metastable solid-solution that is accessible through mechanochemical treatment in planetary mills. (a) ^{19}F MAS NMR spectra (471 MHz) of $(Ca,Sr)F_2$, $(Ba,Sr)F_2$ and $(Ba,Ca)F_2$. *x* refers to the amount of CaF_2 in $Ba_{1-x}Ca_xF_2$. The latter one decomposes at elevated *T*. (b) ^{19}F MAS NMR spectra of selected compositions *x* revealing the distribution of the different cation environments. Inset: Crystal structure of *c*-BaF_2. Chemical shifts refer to C_6F_6. Figures adapted from reference [14]. Asterisks denote spinning sidebands.

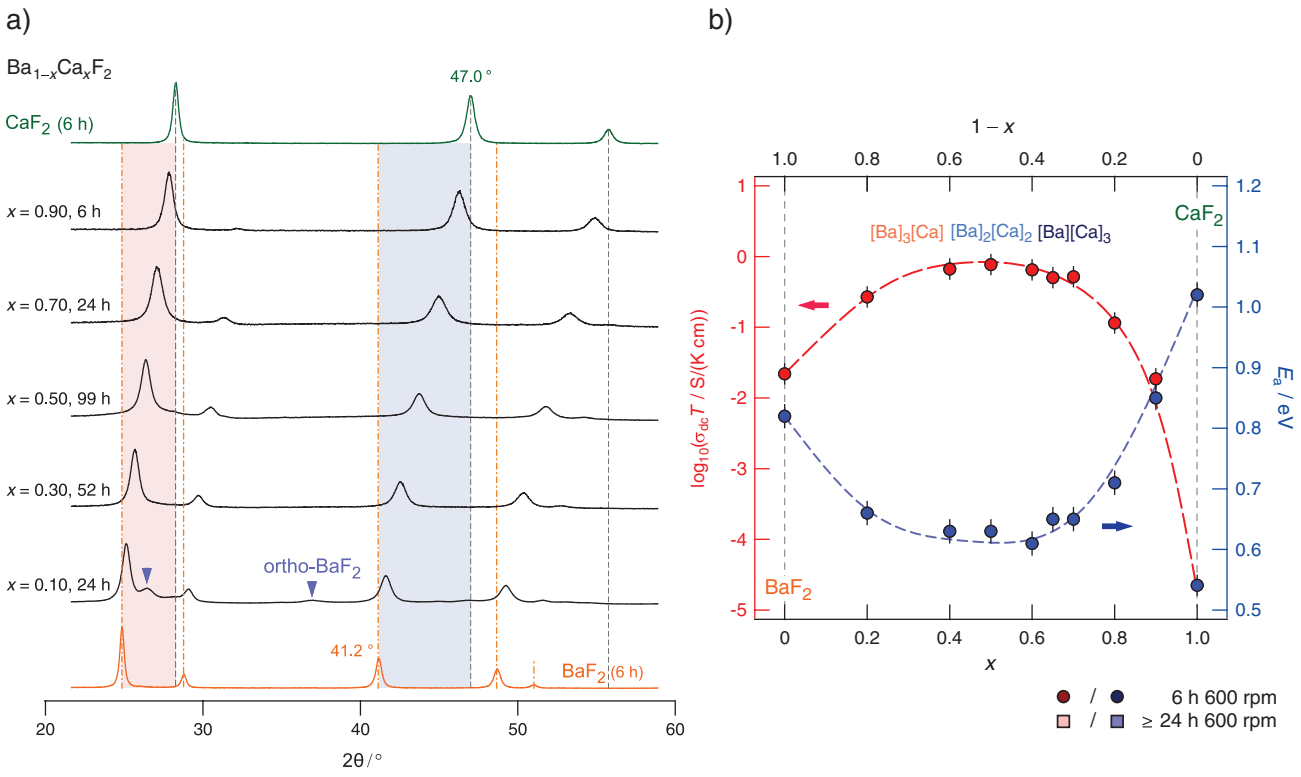

Fig. 4: (a) X-ray powder patterns of $Ba_{1-x}Ca_xF_2$ prepared via mechanical milling the binary fluorides BaF_2 and CaF_2 for the times indicated [14]. The incorporation of smaller Ca^{2+} ions in the BaF_2 lattice causes the reflections to shift toward large diffraction angles. Triangles mark the formation of orthorhombic BaF_2 which is a high-pressure modification of BaF_2. (b) Variation of both the conductivity (read off from the isotherms at low frequencies) and the activation energy with composition *x*.

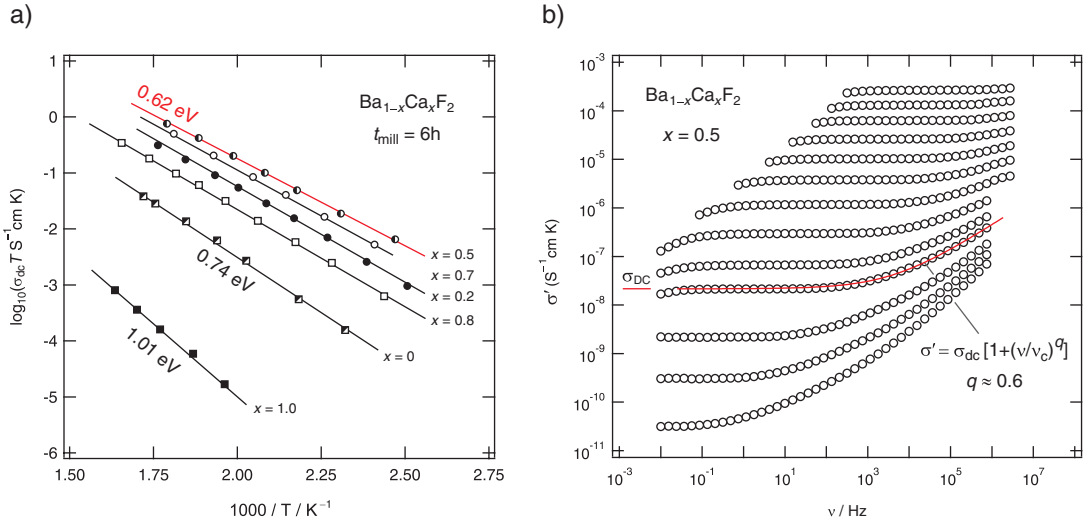

Fig. 5: (a) Arrhenius plot of ionic conductivities of $Ba_{1-x}Ca_xF_2$. The electronic contribution to σ_{dc} is negligible as can be shown through polarisation experiments. (b) Underlying conductivity isotherms of $Ba_{1-x}Ca_xF_2$ used to extract dc ion conductivities. The spectra are composed of a frequency-independent plateau reflecting long-range ion transport and a dispersive contribution at higher frequencies. Piling up of F anions in front of the blocking electrodes used to record the data manifest as decrease in conductivity at low frequencies. Figures adapted from the supplemental material of reference [14].

passes through a maximum at $x = 0.5$; at the same composition the activation energy takes the lowest value, see Figure 4b showing the full picture of ion dynamics in $Ba_{1-x}Ca_xF_2$ [14]. For comparison, ionic conductivities (σ_{dc}) and activation energies (E_a) of the pure end members BaF_2 and CaF_2 are also included in Figure 4b. The end members have also been treated in the same planetary mill to yield nanocrystalline samples. Although ion transport in the non-mixed samples is enhanced compared to the coarse-grained source materials, the additional increase in ion dynamics by two orders of magnitude for mixed $Ba_{1-x}Ca_xF_2$ is quite evident. In nanocrystalline BaF_2 (and CaF_2) facilitated ion dynamics might be largely affected by point defects and interfacial regions introduced during milling. In addition, the isovalent replacement with the smaller Ca^{2+} ions offers another degree of freedom to manipulate ionic hopping in both the bulk as well as *in* and *near* the grain boundary regions. Obviously, mixing influences both the migration enthalpy of the ions to jump to an empty (vacant or interstitial) site as well as the formation enthalpy to create defects in cubic $Ba_{1-x}Ca_xF_2$. Starting from 0.74 eV at $x = 0$, the effective activation energy is reduced to 0.62 eV at $x = 0.5$. For comparison, ion hopping in nanocrystalline, ball-milled CaF_2 is characterized by values as high as 1.01 eV.

The increase in F anion diffusivity is also seen from an atomic scale point of view via ^{19}F (spin-1/2) NMR spin-lattice relaxation (SLR) rate measurements. If induced by hopping processes of the F anions the temperature dependence of the laboratory-frame SLR rate entails information on local activation energies sensed by the jumping ions. In Figure 6 the ^{19}F NMR SLR rates of $Ba_{1-x}Ca_xF_2$, measured with the saturation recovery technique [50, 51], are shown in an Arrhenius diagram. While for temperatures lower than ca. 285 K non-diffusive contributions affect longitudinal recovery of the magnetization, self-diffusion increasingly influences the rates at higher T. In all cases parts of the corresponding low-T flanks are seen. At even higher temperatures the rates are expected to pass through a diffusion-induced rate peak from which quantitative information on jump rates and long-range activation energies could be gathered. This behavior is indicated in Figure 6a by the dashed lines. The low-T flanks, on the other hand, contain information on *local* ion dynamics. Obviously, considering the slopes of these flanks the local hopping barriers the ions are subjected to are quite similar, that is, almost independent of x. The increase in F anion diffusivity, when going from $x = 0$ to $x = 0.5$, as is definitely seen by heterogeneous line narrowing in static ^{19}F NMR spectra, is reflected by an increase of the absolute relaxation rate rather than by a significant reduction of the local barriers. The expected shift of the rate peaks towards lower T, for samples with x around 0.5, can only be explained by an enhanced pre-exponential factor of the underlying Arrhenius relation [49]. Further insight into this

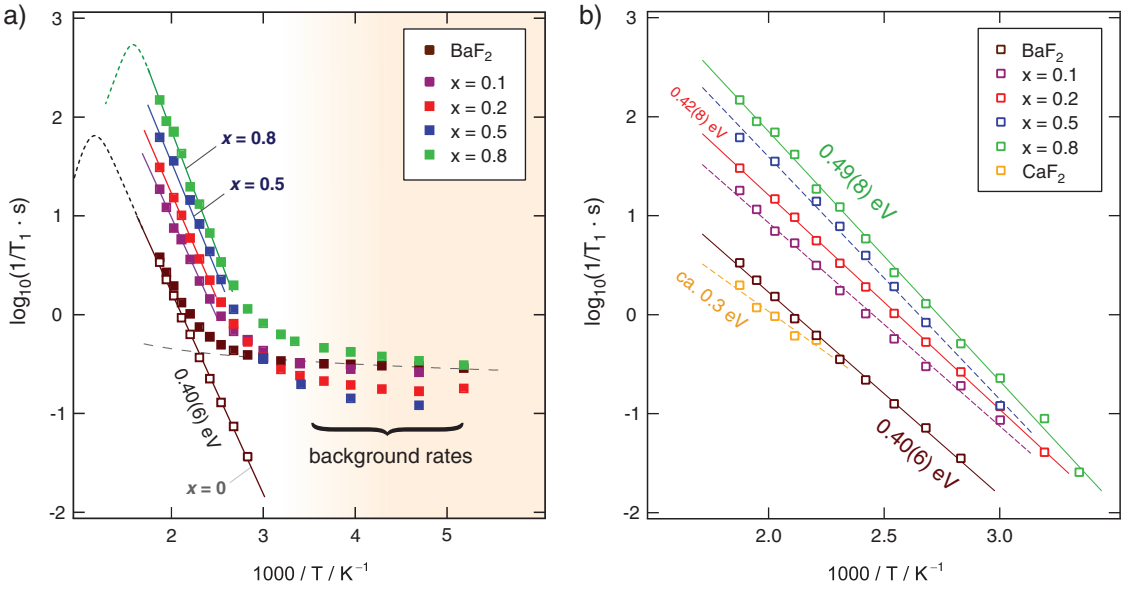

Fig. 6: (a) ^{19}F NMR spin-lattice relaxation rates (282 MHz) of $Ba_{1-x}Ca_xF_2$ revealing diffusion-induced contributions above temperatures as high as 285 K [49]. The solid lines represent fits according to an Arrhenius relation. The dashed line is used to parameterize the non-diffusive background rates; extrapolation of the rates toward higher T and subsequent subtraction yield the purely diffusion induced rates shown as unfilled symbols. These rates are shown in (b) in detail. See text for further explanation.

metastable solid solution is being gained by molecular dynamics simulations and X-ray absorption spectroscopy measurements [52, 53].

Metastable quaternary compounds: Introduction of Sr ions into $BaLiF_3$

As mentioned above, BaF_2 and LiF form the inverse perovskite $BaLiF_3$ when treated in a high-energy ball mill [48]. $BaLiF_3$ is a stable compound that accepts the replacement of some of the Ba ions with Sr ions. Via co-milling of cubic BaF_2 (^{19}F NMR isotropic chemical shift of 152 ppm (C_6F_6 as reference)), SrF_2 (78 ppm) and LiF (–38 ppm) the formation of mixed $(Ba,Sr)LiF_3$ can be followed through X-ray diffraction and ^{19}F MAS NMR as a function of milling time [54]. Whereas the NMR spectrum of the final product, obtained at sufficiently long milling periods, clearly reveals the different F environments composed of Ba and Sr ions (see Figure 7a), at short milling times primarily the formation of orthorhombic o-BaF_2 and $BaLiF_3$ is seen [54]. Note that in o-BaF_2 two magnetically different F sites exist leading to two well separated NMR lines showing up at 103 ppm and 174 ppm if referenced against C_6F_6 (see Figures 7b and 8c). The signal at 66 ppm definitely proves the formation of $BaLiF_3$; in the ternary compound only a single F site is available.

Together with X-ray powder diffraction the following formation mechanism of the quaternary (metastable) compound has been suggested (see also Figure 7b), *cf.* [54]: at first, $BaLiF_3$ is formed into which Sr is increasingly incorporated. At the same time, however, a side reaction takes place that leads to the formation of $(Ba,Sr)F_2$, not shown in Figure 7 but indicated in Figure 8c for $Ba_{0.88}Sr_{0.12}LiF_3$. As observed for $(Ba,Ca)F_2$ and $(Ba,Sr)LiF_3$, the mixed compound $(Ba,Sr)F_2$ shows multiple F sites; the main signal is seen at 120 ppm. Thus, $BaLiF_3$ and, to a minor extent, BaF_2 compete for the incorporation of Sr ions. Since the formation of Ba-free "$SrLiF_3$" (see below) is not observed, any remaining LiF reacts with $(Ba,Sr)F_2$ to form $(Ba,Sr)LiF_3$. The evolution of the 5 NMR lines of $(Ba,Sr)LiF_3$ with increasing milling time t_m (0–20 h) is shown in Figure 7b for the composition $Ba_{0.74}Sr_{0.26}LiF_3$. The area fractions plotted are obtained by deconvolution of the high-resolution NMR spectra with appropriate Voigt functions, as exemplarily shown for two mixtures treated for 30 min and 20 h, respectively.

In order to make the formation of $(Ba,Sr)F_2$ with increasing Sr content visible, ^{19}F MAS NMR spectra were recorded for samples with x ranging from $x = 0.02$ to 0.32, see Figure 8a. The corresponding area fractions of the environments $[Ba]_4$, $[Ba]_3Sr$, $[Ba]_2[Sr]_2$, $[Ba][Sr]_3$ and $[Sr]_4$ in the mixed compound are shown in Figure 8b for a series of samples treated for 20 h in a planetary mill.

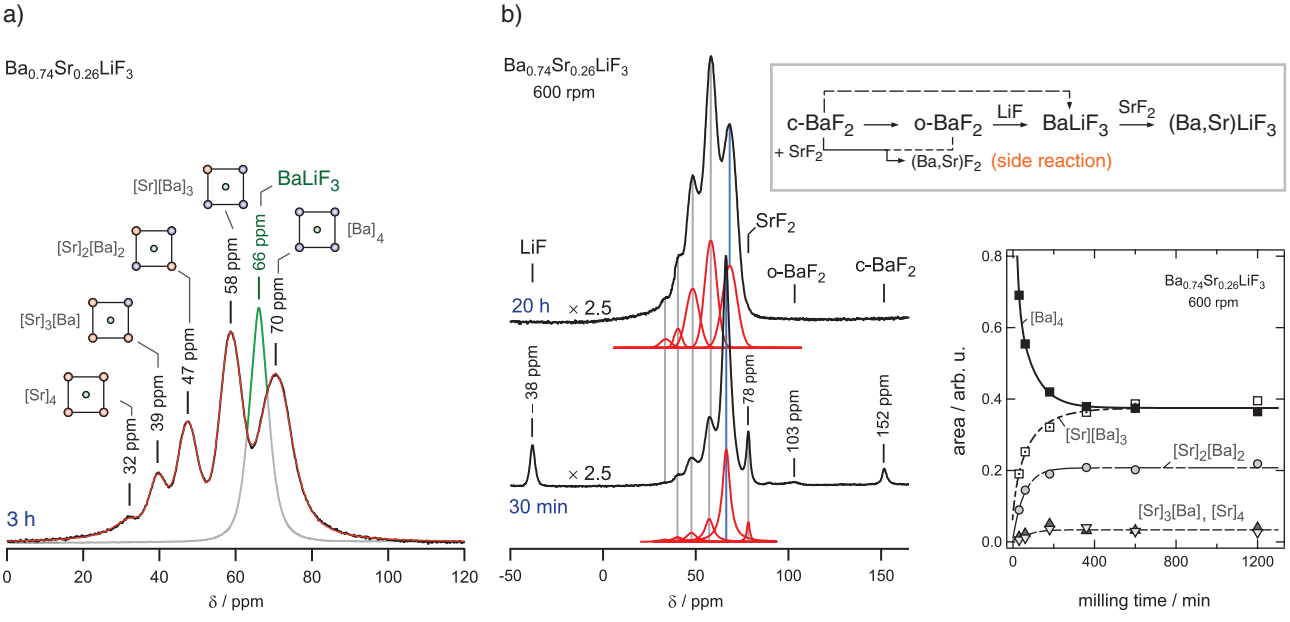

Fig. 7: (a) ^{19}F MAS NMR spectrum (471 MHz) of $Ba_{0.74}Sr_{0.26}LiF_3$ prepared after high-energy ball milling a mixture of BaF_2, SrF_2 and LiF at 600 rpm [54]. The signal of $BaLiF_3$ is located at 66 ppm; while that of the pure $[Ba]_4$ environment in $(Ba,Sr)LiF_3$ shows up at more positive ppm values. (b) Left: Evolution of the ^{19}F MAS spectra with milling time. Solid lines in red show deconvolutions of the different lines of the mixed compounds with Voigt profiles. Right: Change of the areas under the NMR lines of $Ba_{0.74}Sr_{0.26}LiF_3$ with milling time [54]. The formation mechanism proposed is given in the upper part of the figure, see text.

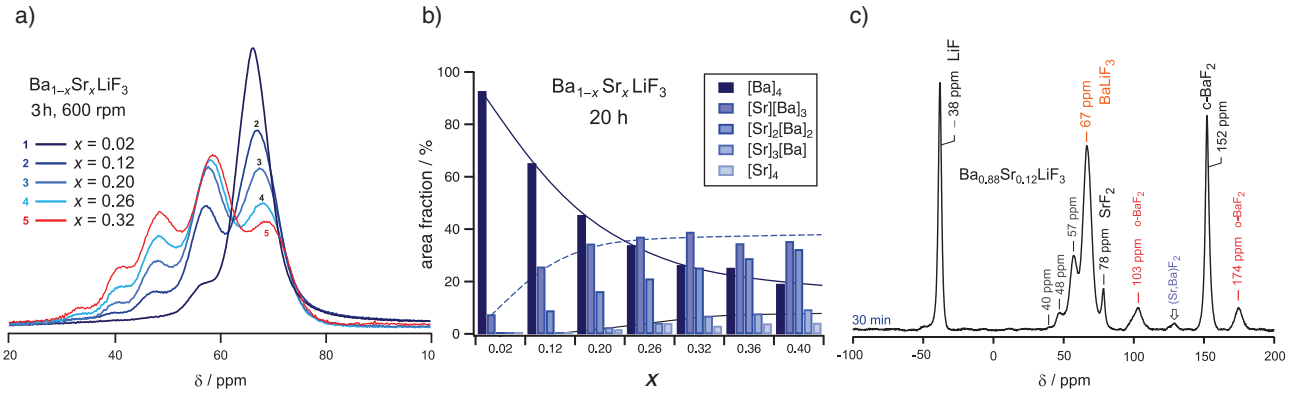

Fig. 8: Formation of metastable (Ba,Sr)LiF_3 as a function of Sr content *x*. (a) Change of the ^{19}F MAS NMR spectra of $Ba_{1-x}Sr_xLiF_3$ with increasing *x*. (b) Corresponding area fractions of the 5 NMR lines seen for mixed (Ba,Sr)LiF_3. (c) ^{19}F MAS NMR spectrum of $Ba_{0.88}Sr_{0.12}LiF_3$ obtained after a milling period of 30 min at 600 rpm. Besides the formation of $BaLiF_3$, orthorhombic BaF_2 (*o*-BaF_2) as well as (Ba,Sr)F_2 show up. Educts such as LiF and *c*-BaF_2 are clearly visible. Further mechanical treatment yields a pure product since solely the ^{19}F NMR lines of (Ba,Sr)LiF_3 are seen. Figures adapted from reference [54].

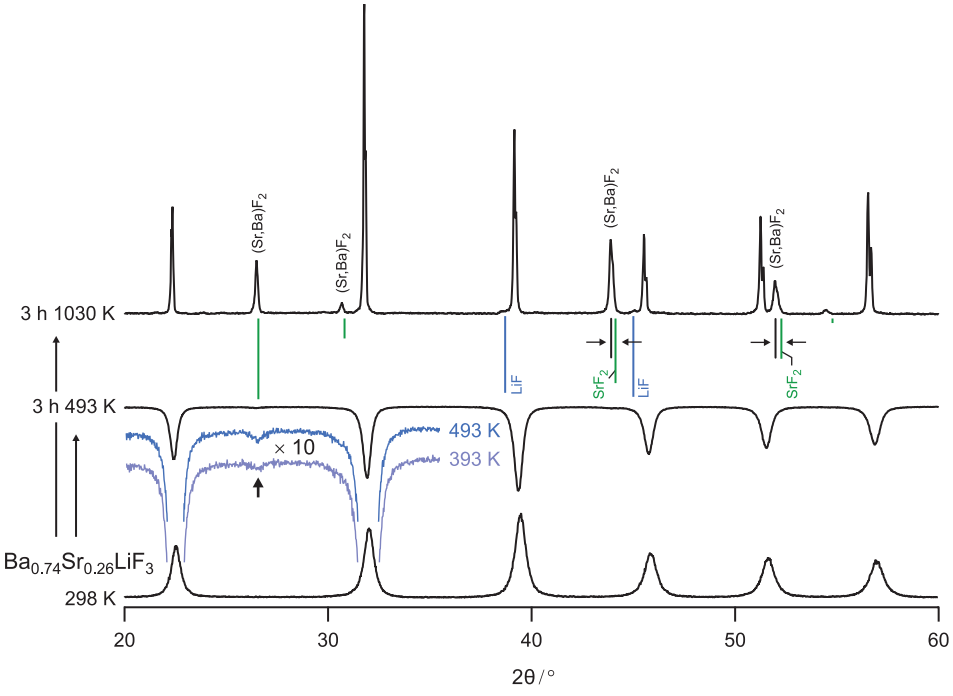

Fig. 9: Change of the X-ray powder diffraction patterns of mechanosynthesized $Ba_{0.74}Sr_{0.26}LiF_3$ upon heat treatment. The results reveal a metastable solid solution that decomposes at higher *T*. Note that X-ray amorphous products can be revealed by ^{19}F NMR spectroscopy, see Figure 10; patterns adapted from reference [54].

$x = 0.4$ represents the upper limit of Sr incorporation at the milling conditions applied. At higher Sr contents the spectra always reveal residual SrF_2 [54].

The amount of Sr, which can be incorporated into $BaLiF_3$ through Ba^{2+} replacement, is in line with the metastability of Sr-rich $Ba_{1-x}Sr_xLiF_3$ observed against heat treatment. As an example, if $Ba_{0.74}Sr_{0.26}LiF_3$ is calcined at 1030 K for 3 h X-ray powder diffraction is composed of sharp reflections that can be assigned to $BaLiF_3$ and SrF_2, (Ba,Sr)F_2 (Figure 9). Close inspection of the diffraction patterns of samples treated at much lower temperatures, however, reveals that the mixed product starts to decompose already under soft annealing conditions (Figure 9, see the magnified patterns obtained after annealing at 493 K and 393 K, respectively). In general, because of the formation of amorphous decomposition products ^{19}F MAS NMR is

extremely helpful in identifying these phases. NMR tells us the $Ba_{0.74}Sr_{0.26}LiF_3$ decomposes into $BaLiF_3$, SrF_2, (Ba,Sr)F_2, *c*-BaF_2 and LiF whereby, for example, LiF is mainly present as an X-ray invisible product (Figures 9 and 10). At soft annealing conditions the amount of (Ba,Sr)F_2 formed is rather low. As is seen via ^{19}F MAS NMR from Figure 10a, already at temperatures as low as 393 K, the characteristic NMR lines of LiF and SrF_2 show up. Since also *c*-BaF_2 is reformed (see Figure 10a), the removal of SrF_2 and LiF from (Ba,Sr)LiF_3 does also affect the remaining Sr-free regions of $BaLiF_3$ that partly decompose into BaF_2 and LiF. Only at much higher temperatures, i.e. through ceramic solid state synthesis, a mixture of BaF_2 and LiF would again yield the inverse perovskite structure with cubic (Ba,Sr)F_2 and LiF as side phases.

Highly conducting fluorite-type solid electrolytes: mixing of *c*-BaF_2 with t-LaF_3

The binary fluorides *c*-BaF_2 (fluorite structure) and *t*-LaF_3 (tysonite structure) are miscible if x in $Ba_{1-x}La_xF_{2+x}$ is kept below $x = 0.55$ and above $x = 0.8$ forming stable solutions up to high temperatures. This circumstance enables both thermal as well as mechanochemical syntheses routes to prepare, for example, cubic-type $Ba_{1-x}La_xF_{2+x}$ [10, 17]. In contrast to solid state synthesis, ball-milling is able to close the miscibility gap [10]. Furthermore, mechanochemically synthesized $Ba_{1-x}La_xF_{2+x}$, obtained without post-annealing, can take advantage of defects (see above) necessary to yield higher conductivities compared to the highly ordered, crystalline counterparts obtained from high-temperature synthesis. Up to ca. $x = 0.78$ the samples crystallize with the fluorite structure, increasing x toward $x = 1$ the structure gradually changes to the tysonite type [10]. In the fluorite region a maximum in conductivity is seen at around $x = 0.4$. With the help of both ac conductivity measurements and ^{19}F NMR relaxometry ion dynamics on both long-range and short-range lengths scales were probed [10, 17, 21]. As an example, ion dynamics in nanocrystalline $Ba_{0.6}La_{0.4}F_{2.4}$ turned out to be rather complex. F anion hopping is governed by a broad range of activation energies with values ranging from 0.16 eV to 0.59 eV [17]. Macroscopic ion transport, to which also dc conductivity measurements are sensitive, turned out to be characterized by 0.59 eV, NMR relaxometry and ac conductivity measurements point to values varying from 0.16 to 0.35 eV. While in Figure 11a the NMR relaxometry response is shown, in Figure 11b broadband conductivity (and permittivity) isotherms are presented able to monitor the change in σ' and ε' over a dynamic range of almost 12 decades [17].

As an example, from the maximum seen when $1/T_{1\rho}$ is plotted vs $1/T$ the self-diffusion coefficient D can be deduced. At 380 K it is in the order of 10^{-14} m^2s^{-1} if a mean jump distance of ca. 3 Å is considered. Assuming uncorrelated motion and a Haven ratio near 1 this value is in line with the dc conductivity, i.e. ac conductivity at very low frequencies, obtained at almost the same temperature [17].

The broad distribution of activation energies manifests itself also in NMR line shapes that reveal dynamically distinct spin reservoirs. If recorded under static

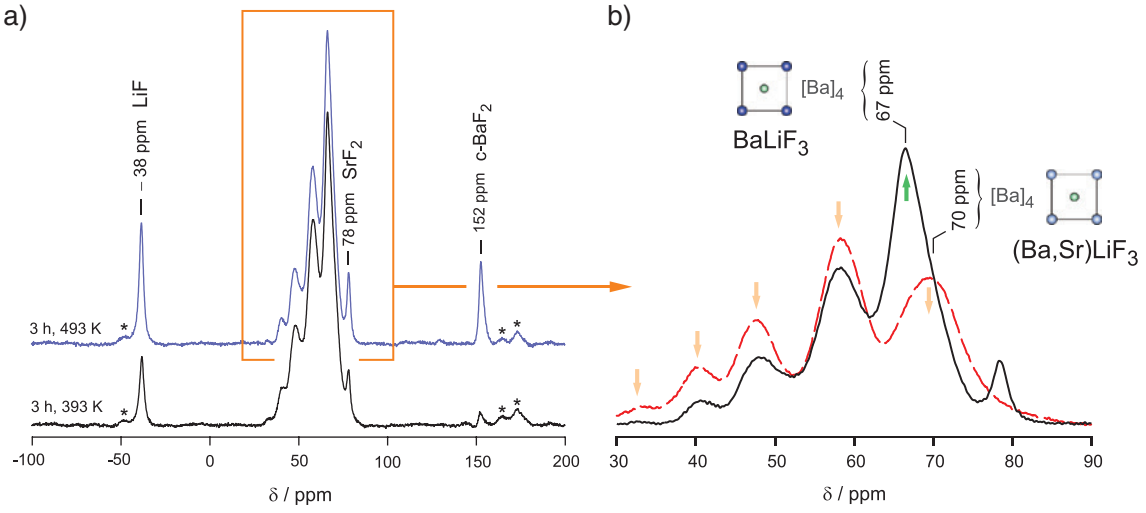

Fig. 10: (a) ^{19}F MAS NMR spectra of $Ba_{0.74}Sr_{0.26}$ heat treated for 3 h at 393 K and 493 K, respectively [54]. The formation of X-ray amorphous LiF and (nanocrystalline) *c*-BaF_2 as well as SrF_2 is clearly visible. Chemical shift refer to the lines of ^{19}F in C_6F_6. (b) Change of the NMR lines of (Ba,Sr)LiF_3 after heat treatment [54]. The line at 67 ppm is attributed to Sr-free $BaLiF_3$. Asterisks denote spinning sidebands.

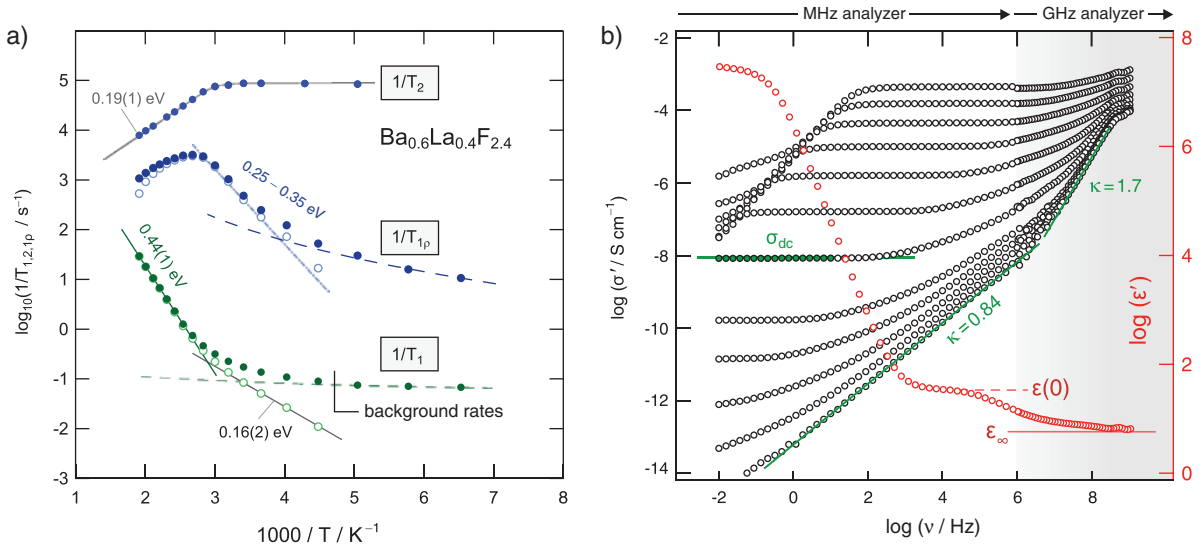

Fig. 11: (a) ^{19}F NMR relaxation rates recorded in the laboratory ($1/T_1$, 282 MHz) and rotating frame of reference ($1/T_{1\rho}$, 62.5 kHz) of nanocrystalline $Ba_{0.6}La_{0.4}F_{2.4}$. Spin-spin-relaxation rates ($1/T_2$) are shown for comparison. The rates contain information on the elementary jump processes of the F anions in the ternary fluoride [17]. (b) Conductivity isotherms recorded from 10^{-2} Hz up to 10^9 Hz (153 K–513 K, in steps of 20 K) [17]. Considering capacities and the mean crystallize of ca. 20 nm one can conclude that the distinct dc plateaus at low frequencies represent bulk response determined by 0.57–0.59 eV; this assignment is corroborated by permittivity values, $\varepsilon(0) < 100$; the curve shown refers to 373 K. While at the very low temperatures strictly localized jump processes might affect σ', at high frequencies interactions with phonons come into play.

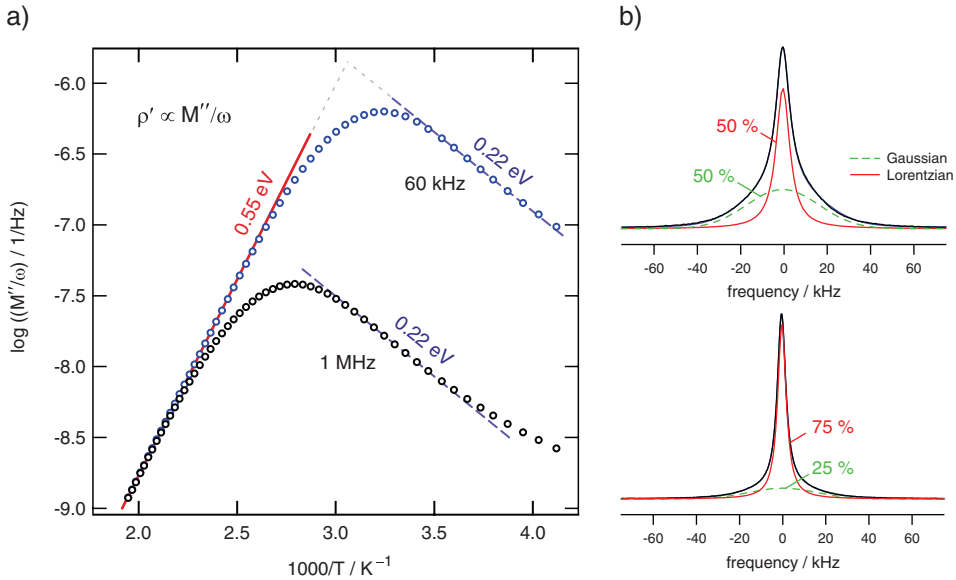

Fig. 12: (a) Real part of the complex resisitivity of $Ba_{0.6}La_{0.4}F_{2.4}$, measured at 1 MHz and 60 kHz, as a function of inverse temperature [17]. Asymmetric peaks are obtained underpinning the idea of heterogeneous ion dynamics: while the low-T sides are governed by an activation energy of only 0.22 eV; on the high-T flank 0.55 eV is obtained. (b) ^{19}F NMR spectra of $Ba_{0.6}La_{0.4}F_{2.4}$ recorded at 323 K (top) and 353 K (bottom) [17]. The lines can be described as the sum of a Gaussian and a Lorentzian (narrow) line.

conditions the ^{19}F NMR lines recorded at different temperatures undergo so-called heterogeneous motional narrowing (see Figure 12b). Narrowing of the line is caused by onset of F ion jump processes with rates exceeding the spectral width of the line at low temperatures. The latter temperature limit is often called the *rigid lattice* regime. In the case of ^{19}F ($I = 1/2$, see above) only dipolar interactions broaden the line; these interactions are averaged leading

to narrowed signals upon heating. Taking into account the energy landscape the ions are subjected to, those having access to low barriers would be responsible for the narrow component, while the less mobile ones cause a broader signal. Interestingly, by plotting the real part of the complex resistivity ρ', which is given by the imaginary part of the electric modulus M'' divided by frequency, as a function of inverse temperature the two limits in activation energy are seen [17]. While the flanks at low T are characterized by 0.22 eV, the high-T flank is governed by 0.55 eV. The observation that E_a values from M'' and σ_{dc} do not vary much points to an almost T independent number density of charge carriers. Remembering the high density of point defects and dislocations introduced through milling, this similarity in activation energies is expected. Figure 13 gives an overview of the conductivities of micro- and nanocrystalline BaF_2 as well as its derivatives by replacing Ba cations with Ca^{2+} or La^{3+} ions.

Channel-structured and layered ternary fluorides: $BaMgF_4$ and $BaSnF_4$

Joint milling of BaF_2 and MgF_2 or SnF_2 leads to the formation of the ternary compounds $BaSnF_4$ and $BaMgF_4$ [18, 19, 55]. While the first shows a layered structure, $BaMgF_4$ crystallizes in the orthorhombic $Cmc2_1$ structure and consists of strands of corner-sharing MgF_6-octahedra that are separated by the Ba-ions [56]. These MgF_6-octahedra run in parallel with the c-axis of the unit cell and provide a 1D pathway which is expected to be the preferred direction of F ion transport [57]. The latter is underpinned by ac impedance spectroscopy: the corresponding conductivity isotherms are composed of a dispersive regime showing a weak frequency dependence [19]. This finding can be interpreted in terms of spatially confined F ion transport [19, 58].

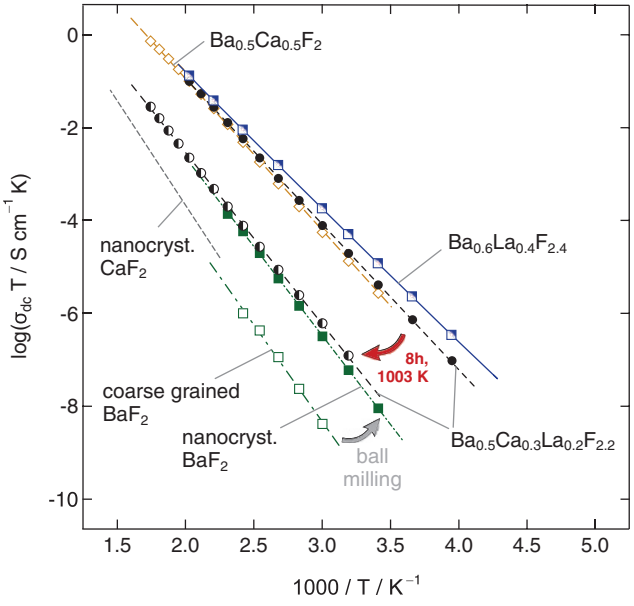

Fig. 13: Overall conductivities of cubic-BaF_2 and its derivatives obtained by iso- or aliovalent replacement of Ba^{2+} with Ca^{2+} or La^{3+} ions. $Ba_{0.6}La_{0.4}F_{2.4}$ and metastable $Ba_{0.5}Ca_{0.5}F_2$ show similar conductivities. Just as $Ba_{0.5}Ca_{0.5}F_2$ the quaternary compound $Ba_{0.5}Ca_{0.3}La_{0.2}F_{2.2}$ does not withstand high temperatures; it decomposes into BaF_2, CaF_2 and La-rich BaF_2 [4].

$BaMgF_4$ usually requires high temperatures to be synthesized from a mixture of BaF_2 and MgF_2 [59, 60]. In the present case it was prepared by means of a planetary ball mill at rotation speeds as high as 1000 rpm. Lower rotation speeds do not lead to the direct formation of the ternary compound [19]. We attribute this finding to the strong heat development at the contact region of the milling media that induces the solid state reaction, finally yielding $BaMgF_4$ as the only phase. The formation of $BaMgF_4$ was followed by both X-ray diffraction and ^{19}F MAS NMR (Figure 14). After 1 h of milling the diffraction pattern reveals the diagnostic reflections of $BaMgF_4$. Only via ^{19}F MAS NMR it was possible to determine the end point of the synthesis. Whereas at milling times shorter than 3 h X-ray amorphous MgF_2 (and BaF_2) is still visible, the NMR spectrum of the sample mechanically treated for 3 h is solely composed of the 4 NMR lines assigned to the magnetically inequivalent F sites in $BaMgF_4$ [19].

The mechanosynthesis of $BaSnF_4$ seems to be only possible through an additional soft annealing step after mechanical activation of the starting materials. During milling BaF_2 and SnF_2 are partly converted into amorphous products; moreover, X-ray diffraction [61] indicates the formation of a metastable Sn-rich BaF_2 phase with cubic symmetry that is transformed into tetragonal $BaSnF_4$ without any by-phases expected for some non-reacted BaF_2 (see Figure 15a and b), *cf.* [18].

Via X-ray diffraction alone it is difficult to assess whether Sn is really incorporated into BaF_2; the patterns obtained show broad asymmetric reflections. Because of the size of the crystallites obtained and the formation of amorphous fluorides ^{19}F MAS NMR spectroscopy might help to identify the product. The similarity of chemical shifts in SnF_2, BaF_2 and the final compound $BaSnF_4$ renders this issue, however, much more difficult than in the case of $BaMgF_4$. The fact that the mixture treated for several hours in a planetary mill easily transforms into tetragonal $BaSnF_4$ could serve as a strong argument that Ba and Sn cations in fact form a metastable, highly disordered compound.

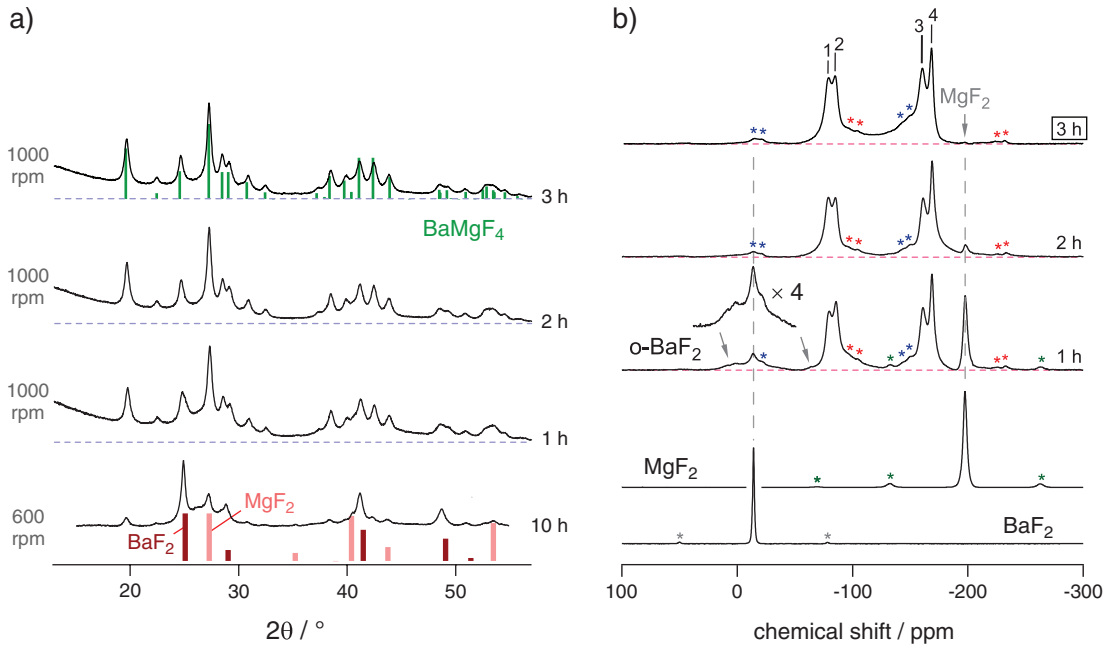

Fig. 14: The formation of $BaMgF_4$ via high-energy ball milling: (a) X-ray diffraction powder patterns and (b) ^{19}F MAS NMR spectra of mixtures of BaF_2 and MgF_2 obtained after the milling times indicated; the spectra of the educts are shown for comparison. Asterisks marks spinning side bands. *o*-BaF_2 reflects BaF_2 with orthorhombic crystal structure. The transformation of *c*-BaF_2 in *o*-BaF_2 is a side reaction; at sufficiently large milling times phase pure $BaMgF_4$ is obtained. Figures adapted from reference [19].

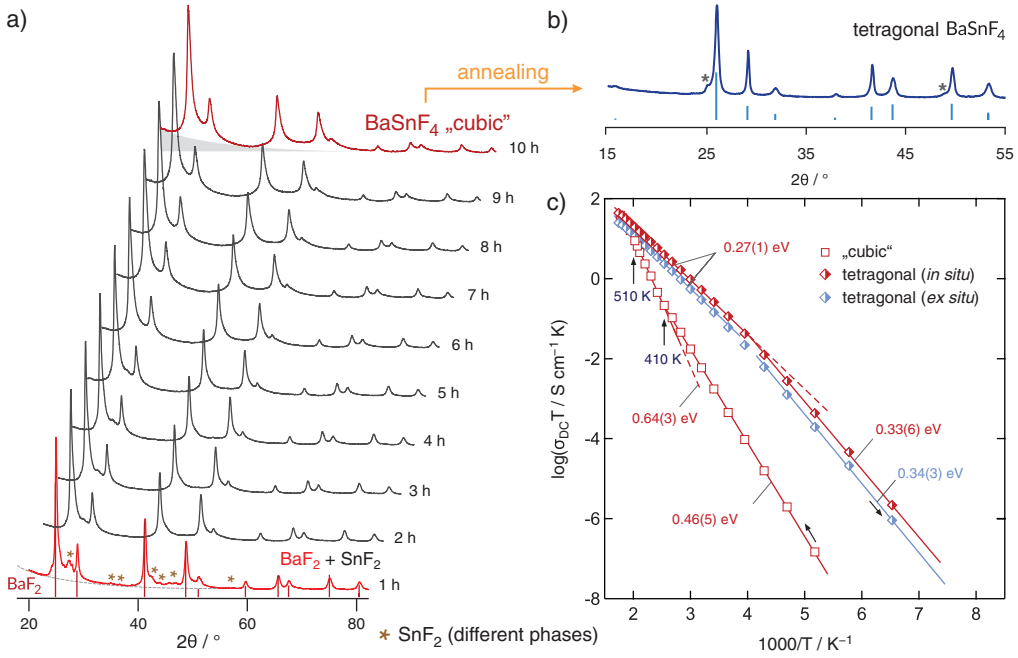

Fig. 15: (a) X-ray powder patterns of BaF_2 mechanically treated together with an equimolar amount of SnF_2. The distinct reflections of SnF_2 disappear with t_{mill}. Annealing at elevated *T* yields tetragonal $BaSnF_4$ (see (b)). (c) Change of conductivity when "cubic" $BaSnF_4$ is transformed into layer structured $BaSnF_4$. The transformation was followed *in situ* as well as *ex situ* by annealing the mixture outside the impedance cell [61]. The different conductivity regimes in $BaSnF_4$ reflect different transport mechanisms.

When annealed at *moderate* temperatures, defects may partly be preserved facilitating ion transport in nanocrystalline, defect-rich $BaSnF_4$ against the coarse-grained counterpart [18] that is available via high-temperature ceramic synthesis routes. The conductivity of the tetragonal modification of $BaSnF_4$ is much higher than that of the "cubic" form (see Figure 15c). $BaSnF_4$ is, besides $PbSnF_4$ [55], known to be one of the fastest F anion conductors (Figure 16) [55, 63–65]. Similar to $BaMgF_4$, it shows anisotropic conduction characteristics. This behavior is related to the alternating double-layer structure of $BaSnF_4$ yielding three different types of interlayers built up of either Ba-Ba, Ba-Sn, or Sn-Sn cations. The F anions are distributed between these layers and participate in differently fast transport processes. Those that are located near the Sn-rich interlayers have access to fast ion transport along the Sn-Sn sheets of the fluoride (Figure 16).

Aliovalent replacement of Ba^{2+} by Rb^+ or La^{3+}, which either creates F vacancies or F interstitials by increasing the number density of charge carriers, serves as a possibility to influence F ion dynamics of $BaSnF_4$. As is shown in Figure 16 for M = Rb, vacant F4 and F3 sites are expected to be generated that might facilitate ion transport in the Ba-rich regions, that is, enabling enhanced ion exchange across the Sn-Sn and Ba-Ba-layers. Preliminary measurements [61] have shown that it is possible to replace at least 0.1 formula units by RbF. $Ba_{0.9}Rb_{0.1}SnF_{3.9}$ indeed shows higher conductivities than $BaSnF_4$, see Figure 17a for a comparison with results from Réau et al. [66], Dénès et al. [63] and Chadwick et al. [67] If the amount of RbF is increased too much, i.e. if it exceeds $x = 0.2$, RbF cannot be incorporated into $BaSnF_4$ any longer, see the reflections in Figure 16.

For $Ba_{0.95}Sr_{0.05}SnF_4$ the increase in ionic conductivity is clearly lower compared to aliovalent doping which affects the defect chemistry (Figure 17a). The enhancement seen is related to the mismatch in ionic radii, the same situation is found for (Ba,M)F_2 (M = Sr, Ca), as discussed above. Interestingly, for $Ba_{0.9}La_{0.1}SnF_{4.1}$ no increase is seen if mechanosynthesized non-substituted $BaSnF_4$ is used as a benchmark. Hence, F ions on interstitial positions seem to be less mobile than those having access to vacant anion sites in the F sub-lattice. With regard to the front runner $PbSnF_4$ (see Figure 17b), $Ba_{0.9}Rb_{0.1}SnF_{3.9}$ shows very similar ion dynamics at temperatures near ambient making it a powerful new ionic electrolyte.

Complex oxides with local non-equilibrium structures

In this section, the richness of heterogeneous mechanochemical processes to prepare complex *oxides* of different families, such as stannates (Zn_2SnO_4) [68], silicates (Fe_2SiO_4) [69], ferrites ($BaFe_{12}O_{19}$ and $BiFeO_3$) [70–72], with a variety of structure types (spinel, olivine, hexagonal, perovskite) are exemplified. The examples demonstrate that these oxides can be mechanosynthesized at ambient temperature directly from their precursors in the form of powders with nm-sized crystallites. There is no need for calcination at intermediate temperatures, as mentioned above. This fact makes the process very simple and cost-effective. Selected examples showing functional, e.g. magnetic, properties, metastability and a high reactivity of mechanosynthesized oxides will be briefly discussed. The examples shown also include the transformation of

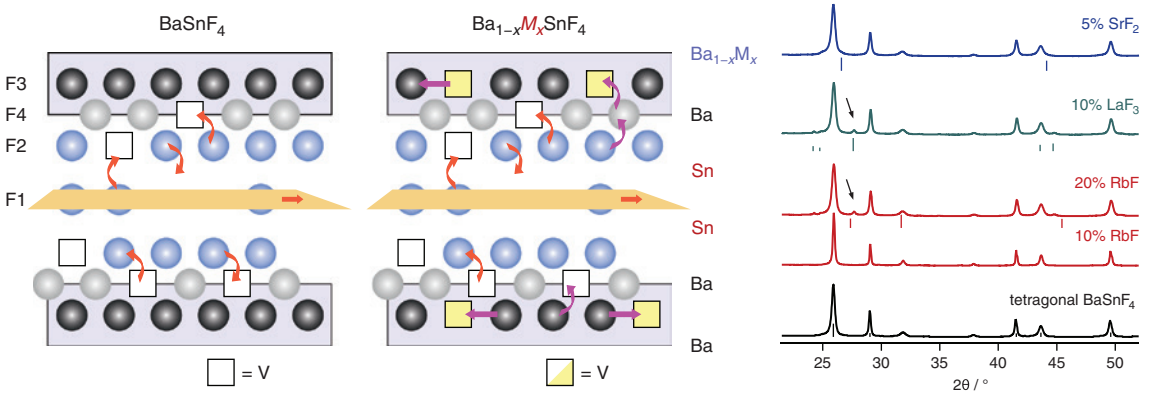

Fig. 16: (Left) Schematic structure of the layered compound $BaSnF_4$ indicating the prevailing hopping processes suggested by Grey and co-workers [62]: fast ion transport along the sheets and slower F exchange perpendicular to them. (Middle) Creation of vacancies in the Ba-rich layers might facilitate ion hooping in these regions leading to an enhancement of ion conductivity. (Right) X-ray powder patterns of $BaSnF_4$ into which Rb^+, Sr^{2+}, and La^{3+} has been incorporated. The maximum allowed value for $Ba_{1-x}Rb_xSnF_{4-x}$ is well below $x = 0.2$. Note that $Ba_{0.9}Rb_{0.1}SnF_{3.9}$ yields an X-ray powder pattern without any reflections of residual RbF.

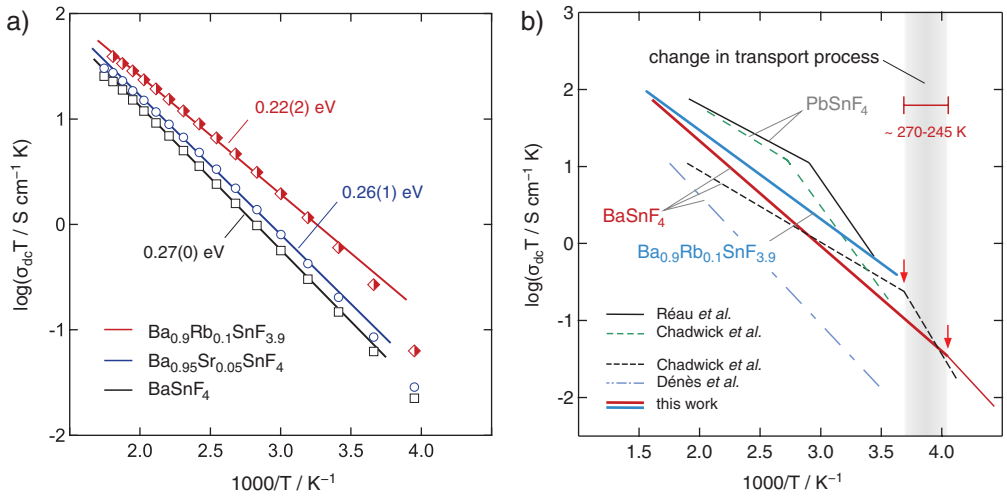

Fig. 17: (a) Change of the conductivity of $BaSnF_4$ when Sr^{2+}or Rb^+ ions are replaced for the divalent Ba^{2+} cations in $BaSnF_4$. From the Arrhenius plot activation energies ranging from 0.22 eV to 0.27 eV were deduced [61]. (b) Comparison of the conductivities of mechanosynthesized $BaSnF_4$, see reference [18], and $Ba_{0.9}Rb_{0.1}SnF_{3.9}$ with those of $BaSnF_4$ and $PbSnF_4$ prepared via conventional solid state synthesis. Some authors report on a change of the transport process at approximately 270 K. This change might be attributed to anisotropic dynamics in layered $BaSnF_4$, see also [62]. *Cf.* text for bibliographical references.

γ-Al_2O_3 into the thermodynamically more stable α-form through mechanical treatment under dry conditions [73], ^{27}Al MAS NMR revealed that metastable nanocrystalline γ-Al_2O_3 can be prepared with an extraordinary large number density of penta-coordinated Al sites, which, most likely, are located mainly on the surfaces of the particles.

Mechanosynthesized Zn_2SnO_4 with metastable cation distribution

As an introductory example, in Figure 18 the mechanosynthesis of zinc stannate from a mixture of binary oxides according to $2\,ZnO + SnO_2 \rightarrow Zn_2SnO_4$ is illustrated [68]. The reaction was followed by XRD and ^{119}Sn MAS NMR in detail [68]. As can be clearly seen, in the XRD pattern of the mixture milled for 4 h, all diffraction peaks detected can be ascribed to the Zn_2SnO_4 phase. Similarly, after 4 h of milling, the resonance peak at −604 ppm, which reflects the Sn atoms located in the SnO_6 octahedra in the tetragonal structure of the SnO_2 educt, has completely disappeared; see Figure 18, right. The corresponding MAS NMR spectrum of the milled powder is dominated by the lines assigned to the Sn^{4+} cations in the spinel structure of Zn_2SnO_4. For comparison, the XRD pattern and the NMR spectrum of the Zn_2SnO_4 reference sample – the bulk material was prepared by means of conventional ceramic routes – are also presented at the bottom of Figure 18. In contrast to the relatively narrow reflections in X-ray powder diffraction of bulk Zn_2SnO_4, the broadened ones

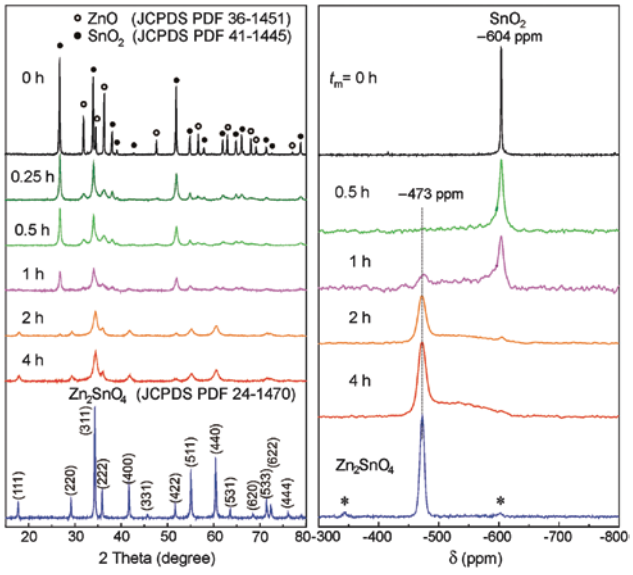

Fig. 18: (left) XRD patterns and (right) ^{119}Sn MAS NMR spectra of the $2ZnO + SnO_2$ mixture milled for various times (up to 4 h) and of (bottom) the bulk Zn_2SnO_4 prepared by the conventional ceramic route. The mechanosynthesis was performed in a Pulverisette 7 planetary mill. The milling times are shown in the figure. Diffraction peaks of the bulk Zn_2SnO_4 are denoted by Miller indices. Spinning sidebands associated with the resonance at – 473 ppm are marked with asterisks. Figure adapted from ref. [68].

of the mechanosynthesized stannate provides clear evidence of its nanoscale nature.

The complementary methodological approach, i.e. the application of a variety of spectroscopic techniques,

allowed for a systematic investigation of structural disorder of mechanosynthesized oxide nanoparticles at the atomic level [68, 69, 71, 72, 74–77]. For example, the comparative ^{119}Sn MAS NMR and Raman spectroscopic studies of bulk and nanocrystalline Zn_2SnO_4 enabled us to separate surface effects from bulk effects of the nanoparticles [68]. While the inner core is found to possess the *fully inverse* spinel structure of the type $(Zn)[SnZn]O_4$ with the regular geometry of constitutive polyhedra, the surface shell is disordered due to a non-equilibrium cation distribution. Because of this distribution a *partly inverse* spinel structure of the type $(Zn_\lambda Sn_{1-\lambda})[Sn_\lambda Zn_{2-\lambda}]O_4$ is formed that is characterized by a broadly distorted local environment around the cations [68]. Here, λ represents the so-called *degree of inversion*, which describes the distribution of cations over the sites of tetrahedral (A) and octahedral (B) coordination provided by the spinel structure.

Orthorhombic α-Fe_2SiO_4

The next example deals with the mechanosynthesized orthorhombic α-Fe_2SiO_4 phase (the so-called *fayalite*) with the olivine structure, prepared from the starting $2\,\alpha\text{-}Fe_2O_3 + 2\,Fe + 3\,SiO_2$ mixture. The mechanochemical processing of these three reactants generates a complex series of heterogeneous solid-state transformations, including redox reaction ($2\,Fe^{3+} + 2\,Fe^0 \rightarrow 3\,Fe^{2+}$) and formation reaction ($2\,\alpha\text{-}Fe_2O_3 + 2\,Fe + 3\,SiO_2 \rightarrow 3\,\alpha\text{-}Fe_2SiO_4$) completed after only 4 h [69]. In this case, ^{57}Fe Mössbauer spectroscopy even allows a quantitative determination of the distribution of Fe^{2+} cations within the core (with regular and asymmetric octahedra) and shell (with distorted albeit more symmetric octahedra) of mechanosynthesized nanoparticles. The spectrum of the bulk silicate (Figure 19, top) is well fitted by the superposition of two doublets, consistent with the olivine crystal structure of α-Fe_2SiO_4, in which Fe^{2+} cations occupy two non-equivalent octahedral sites, [M1] and [M2], in equal proportions, whereas Si^{4+} cations are coordinated by four O^{2-} ions to form SiO_4 tetrahedra (T). Thus, the crystal chemical formula emphasizing the site occupancy at the atomic level in bulk α-Fe_2SiO_4 may be written as $[Fe]_{[M1]}[Fe]_{[M2]}Si_{(T)}O_4$. On the other hand, the core–shell morphology of mechanosynthesized nanoparticles requires to fit their Mössbauer spectrum by a superposition of four sub-spectra (Figure 19, bottom): two components account for Fe^{2+} nuclei in the well-crystallized core of Fe_2SiO_4 nanoparticles (denoted [M1]c and [M2]c) and two are associated with Fe^{2+} ions in the surface shell/interface regions of nanoparticles (denoted [M1]s and [M2]s, *cf.* [69]). As it is seen in Figure 19, the Mössbauer lines corresponding to Fe atoms

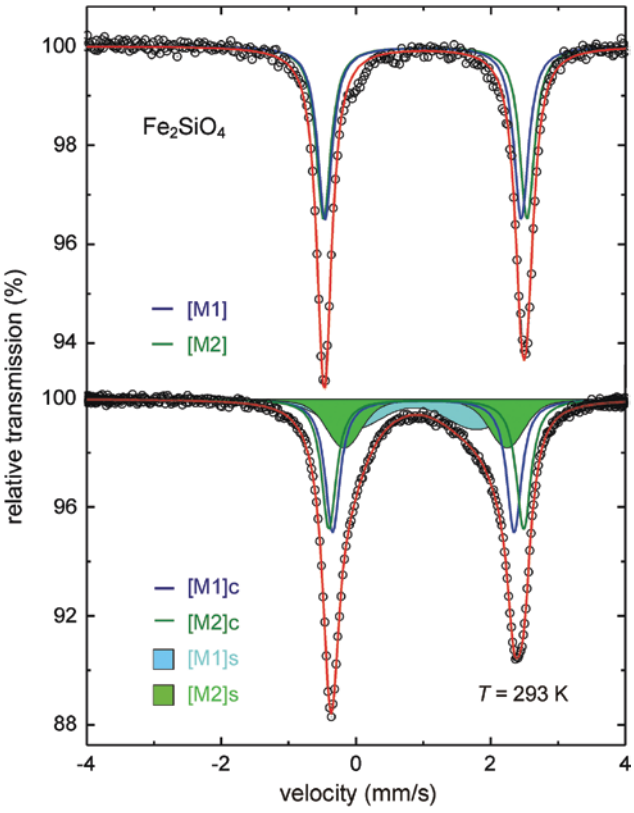

Fig. 19: Room-temperature ^{57}Fe Mössbauer spectra of (top) bulk α-Fe_2SiO_4 and (bottom) nanosized mechanosynthesized α-Fe_2SiO_4 with the olivine structure. [M1]c, [M2]c and [M1]s, [M2]s denote cation sites of octahedral coordination in the inner core and the surface shell of α-Fe_2SiO_4 nanoparticles, respectively. Figure adapted from reference [69].

located at surfaces/interfaces are much broader than those belonging to the core of nanoparticles. This provides clear evidence of a broad distribution of electric field gradients acting at the Fe^{2+} nuclei in the near-surface layers/interface regions of the mechanosynthesized material. The distribution reflects the presence of strongly distorted octahedra around the ferrous ions in the surface/interface regions of the nanofayalite.

Another striking feature is that the electric field gradients which act on Fe nuclei in the shell are found to be smaller than those experienced by Fe nuclei in the core of Fe_2SiO_4 nanoparticles [69]. This indicates that [M1] and [M2] octahedra in the surface shell regions of mechanosynthesized fayalite nanoparticles are more symmetric (with a reduced dispersion of Fe–O bond lengths) than those in the core of nanoparticles. On another hand, the Mössbauer subspectra corresponding to the shell are broader than those associated with the core, reflecting the presence of broadly distorted octahedra in the surface shell. Thus, from Mössbauer measurements it is concluded that

the surface shell regions of mechanosynthesized nanoparticles are disordered due to broadly distorted albeit more symmetric octahedra.

The far-from-equilibrium structural state of the mechanically prepared oxide phases has significant implications for their functional properties. This is exemplarily demonstrated in Figure 20, which compares the magnetization hysteresis loops measured at 5 K for bulk and mechanochemically prepared $BaFe_{12}O_{19}$ with various crystallite sizes (D) [72]. It is found that the saturation magnetization of $BaFe_{12}O_{19}$ decreases with decreasing crystallite size from ca. 69 emu g^{-1} (for bulk $BaFe_{12}O_{19}$ with $D = 220$ nm) to ca. 30 emu g^{-1} (for nanoferrite with $D = 14$ nm). On the other hand, the coercive field of the nanomaterial is about 34% larger than that of the bulk sample. Obviously, these large variations in magnetization and coercivity offer an ample opportunity to manipulate and tailor the functional properties of this magnetically hard material. The macroscopic magnetic behavior of the mechanochemically prepared $BaFe_{12}O_{19}$ is attributed to the effects of the mechanically induced far-from-equilibrium structural disorder, which is located in the interface/surface regions of the nanoferrite [72].

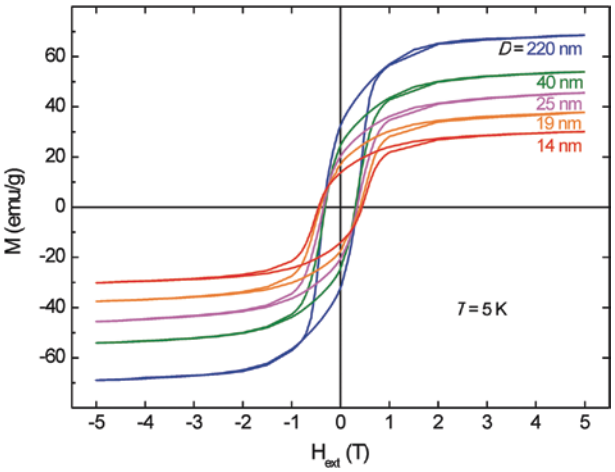

Fig. 20: Magnetization hysteresis loops for bulk and nanoscale mechanochemically prepared $BaFe_{12}O_{19}$ with various crystallite sizes (D). Hysteresis loops were measured at 5 K after field cooling with the external magnetic field of 5 T. The average crystallite sizes of the as-prepared $BaFe_{12}O_{19}$ samples are shown in the figure. Illustration taken from reference [72].

Nanostructured $BiFeO_3$

The next example presented is related to the *stability* of mechanosynthesized nanooxides at changing environments in which these nanostructures are expected to operate. The stability of mechanosynthesized nanoparticles is determined to a large extent by the nature of structural disorder of their near-surface/interface regions [3]. In the case of amorphous surfaces/interfaces such as those detected in mechanosynthesized $BiFeO_3$ [71], the nanomaterial is found to respond even to a small change of environment in the course of TEM investigations. Figure 21 documents the rapid kinetics of the electron beam-induced crystallization of the near-surface layers of mechanosynthesized $BiFeO_3$ perovskite observed at *in situ* conditions [71]. This finding can be interpreted as a

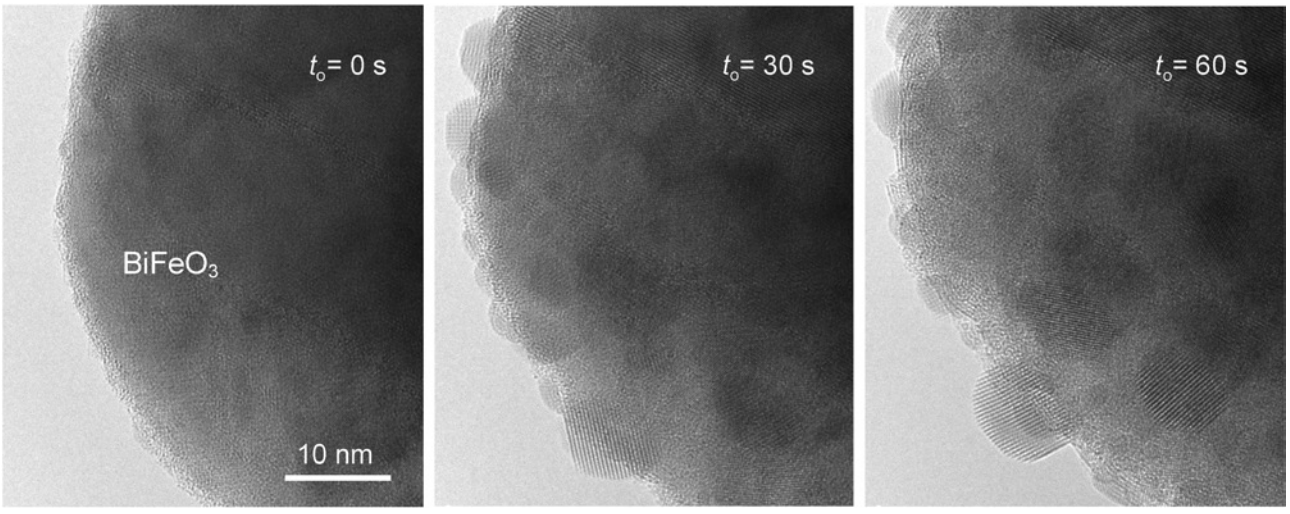

Fig. 21: *In situ* high-resolution TEM observation of the crystallization of the amorphous near-surface layers of mechanosynthesized $BiFeO_3$ perovskite. The metastability of the mechanically induced high-energy surface states manifests itself by the rapid crystallization reaction on the electron irradiation in the course of TEM investigations. The observation time (t_0) is shown in the figure. Figure taken from reference [70].

reaction of the mechanically induced high-energy surface states to electron irradiation. This observation demonstrates both the inherent instability and the high reactivity of "fresh" mechanosynthesized surfaces.

Based on the analogy with the electron beam-induced nucleation and growth processes presented above, we can state that the structurally disordered (amorphous) surfaces or interfaces play an essential role in the mechanically induced formation reactions; the impact-induced nucleation and growth processes of the mechanosynthesized phase are spatially confined to these highly deformed regions [3, 70, 71]. During the early stages of high-energy ball milling the reaction precursors are mixed at the atomic level and a new phase nucleates at the interfacial regions between the solid reactants during the impact period. The growth mechanism of the nuclei or the initial crystallites of the new phase could be understood as the result of the competitive effects of the impact-induced local heating and strains. The latter are accompanied by amorphization, i.e. formation of structurally disordered regions, of repeatedly impacted surfaces whereas the involved "thermal spikes" cause their crystallization [3, 70, 71]. Thus, the mechanism of mechanosynthesis of non-equilibrium oxide phases has been interpreted as being due to "nucleation-and-growth" processes starting from the amorphous phase.

Nanocrystalline Al_2O_3 with catalytically active, penta-coordinated Al sites

The last example presented focuses on the transformation of γ-Al_2O_3 into the thermodynamically more stable α-modification through mechanical action [73]. The transformation can be induced by mechanical treatment in planetary or shaker mills. Depending on the various milling conditions that can be utilized to prepare nanocrystalline ceramics, intermediates can be isolated. The X-ray powder diffraction pattern of the intermediate when γ-Al_2O_3 is treated for a short period of time, e.g. for 5 h, in planetary mills is shown in Figure 22a.

The formation of extended regions of crystalline α-Al_2O_3 does not take place as can be underpinned by ^{27}Al MAS NMR spectroscopy. While X-ray powder diffraction measurements suffer from structural disorder present, local coordination spheres of the Al cations can be well-resolved by NMR techniques particularly when carried out at large spinning speeds and high magnetic fields.

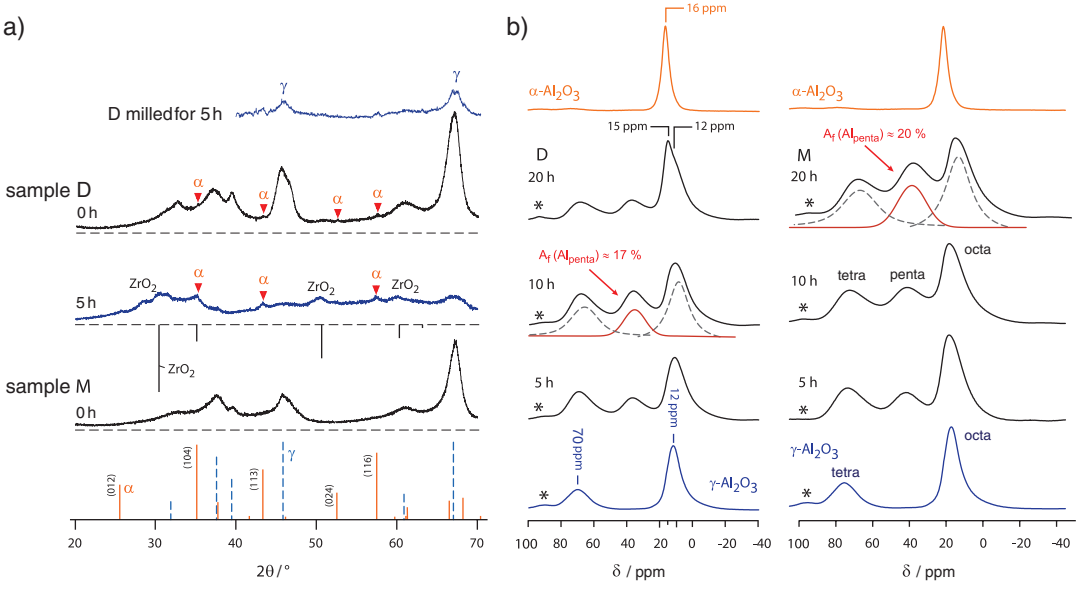

Fig. 22: (a) X-ray powder diffraction of γ-Al_2O_3 purchased from two suppliers viz. Merck (M, purity > 99.5 %, BET surface area 126 $m^2\,g^{-1}$) and Dalian Luming Nanometer Materials Ltd. (99.99 %, 144 $m^2\,g^{-1}$). Reflections assigned to ZrO_2 originate from abrasion during milling in zirconia vials. The formation of crystalline α-Al_2O_3 is hardly seen via X-ray diffraction; ^{27}Al MAS NMR helps identify amorphous phases formed, see (b) [73]. The ^{27}Al MAS NMR spectra of the starting material (shown at the bottom) reveal octahedrally and tetrahedrally coordinated Al cations as expected. With increasing milling time of up to 10 h the signal at 70 ppm remains almost unaffected pointing to Al ions subjected to local environments being identical or resembling that of γ-Al_2O_3 [73]. Most interestingly, mechanical treatment using short milling times does not significantly induce the γ-α phase transformation but leads to the generation of penta-coordinated, unsaturated Al cations that may act as anchoring sites for catalytically active materials such as Pt [78, 79]. These sites are represented by the line at ca. 70 ppm. See text for further explanation.

In γ-Al_2O_3 the Al cations are distributed over two crystallographically distinct sites being coordinated either by six or four oxygen atoms. Hence, the ^{27}Al MAS NMR spectrum is composed of two lines showing up at 12 ppm (AlO_6 octahedra) and at ca. 70 ppm (AlO_4 tetrahedra). Mechanical treatment attacks the surface of the Al_2O_3 particles and causes the formation of unsaturated Al sites with five oxygen ions in the direct neighborhood [73]. While the signal at 70 ppm is still clearly visible after milling the samples for 5 h and 10 h, an additional line at approximately 40 ppm evolves that is a direct proof for the AlO_5 environments [80]. AlO_5 units of the Al_2O_3 substrate may act as anchoring sites for catalytically active metals such as Pt [78, 79, 81]. The area faction A_f of this site amounts to ca. 20 % if sample M is milled for 20 h, see Figure 22b.

Heat treatment and milling for extremely long time promotes the γ-α phase transformation finally yielding the α-polymorph. A systematic study of the influence of the various milling conditions on the phase transformation induced by mechanical action showed that the underlying mechanism is presumably similar to that reported for the thermally induced transformation [82, 83], i.e. the growth of α-Al_2O_3 starts from the unsaturated Al centers on the surface of a metastable γ-Al_2O_3 crystallite and propagates into the inner regions [73]. Worth noting, when the initially formed penta-coordinated Al centers are immediately trapped after they have formed, e.g. by adding CaF_2, the initialization of the transformation can be largely suppressed [73]. This clearly illustrates the important role of unsaturated Al ions against, e.g. the effect of seed crystals.

It turned out that the presence of α-Al_2O_3 seed crystals, either added or already present in the starting material, seem to play neither the major nor the only role in driving the transformation [73], Instead, the main reasons for a complete phase transformation have to be looked for in the very early stages of milling. Obviously, the initial surface area of the starting material takes a decisive part. The smaller the surface area of the crystallites, that is, the larger the crystallites of the starting material are, the easier the phase transformation takes place. Presumably, this is due to the fact that the γ-modification of Al_2O_3 becomes stabilized when the mean crystallite size falls below a certain limit. Thus, at least two competitive processes influence the γ-α transformation: (i) mechanical treatment (ii) induces the formation of α-Al_2O_3, but, at the same time, (ii) ensuring that nanostructuring of the material stabilizes the γ-modification. Altogether, the various milling conditions (the type of the mill used, the milling vial, the ball-to-powder ratio) can be adjusted such that the result of the milling process yields metastable compounds with defined number densities of penta-coordinated Al sites in the surface-influenced volume of the ceramic [73].

Summary and outlook

Mechanochemistry offers versatile possibilities to synthesize complex fluorides and oxides that may benefit from new and unusual properties of the nm-sized crystallites. These properties are related to (i) large surface areas, (ii) macro- and microscopic structural disorder including the formation of point defects, as well as (iii) thermodynamic metastability or, in other words, the preparation of non-equilibrium phases. Mechanosynthesis is controlled by a complex interplay of the materials properties and the external milling conditions. Nevertheless, it represents a highly effective tool to isolate (metastable) compounds which are not available by, e.g. conventional synthesis routes requiring high temperatures or by wet chemical routes. The possibility to stop the milling process at any time offers the chance to freeze the reaction which enabled us to study the underlying formation mechanisms and properties of intermediates *quasi in situ*.

In this short review we have spotlighted recently studied fluorides and oxides to (systematically) understand the conditions under which they form. Mechanical treatment of binary fluorides or oxides in high-energy ball mills (under dry conditions) force the reactants to form compounds that would not be stable at ambient temperatures, some of them need extraordinary high temperatures to exist. Under the harsh conditions of preparation also *local* non-equilibrium and defect-rich structures can be preserved at ambient temperatures. The properties of the compounds obtained, being of electric or magnetic nature, are governed either by non-equilibrium structures, see $Ba_{1-x}Ca_xF_2$, $Ba_{1-x}Sr_xLiF_3$, Zn_2SnO_4, or Fe_2SiO_4, or by an over-proportionally high number density of defects and coordination spheres that are introduced during milling, see $BaSnF_4$, $Ba_{1-x}La_xF_{2+x}$, γ-Al_2O_3. The latter example, together with the HR-TEM investigations on perovskite-type $BiFeO_3$, reveal the high reactivity of the surface states of mechanosynthesized nanocrystalline ceramics. Considering ion dynamics, such high-energy states will of course largely influence ion (and electron) dynamics in compounds prepared by ball milling. Correlating ion transport properties and self-diffusion parameters from both conductivity and NMR spectroscopy with the local non-equilibrium structures, as deduced, e.g. through high-resolution ^{19}F MAS NMR spectroscopy, characterizes the long-term goal of the present study. The knowledge generated will help us to

tune materials properties and, with the help of the architectural rules deduced, to prepare new materials with predefined features. Further studies will keep track of this target by employing also other diffraction techniques, such as extended X-ray absorption fine structure measurements, and by extending our NMR experiments towards nuclei such as ^{135,137}Ba, ^{119}Sn or ^{139}La; the corresponding experiments are currently running in our labs.

Acknowledgments: This short review on mechanosynthesized fluorides and oxides includes selected examples of our studies over the last 6 years (2010–2016) that were funded by the Deutsche Forschungsgemeinschaft (DFG) in the frame of the Priority Programme SPP 1415. We thank our colleagues in Hannover, Karlsruhe and Graz for their help and valuable discussions in achieving the goals of the joint project called "Mechanochemistry of non-equilibrium oxide and fluoride phases: mechanosynthesis, solid state kinetics and spectroscopic properties". Furthermore, the authors thank Professor K. D. Becker for his continuous and supporting interest in their work. Financial support by the DFG is greatly appreciated.

References

[1] S. L. James, C. J. Adams, C. Bolm, D. Braga, P. Collier, T. Friscic, F. Grepioni, K. D. Harris, G. Hyett, W. Jones, A. Krebs, J. Mack, L. Maini, A. G. Orpen, I. P. Parkin, W. C. Shearouse, J. W. Steed, D. C. Waddell, Mechanochemistry: opportunities for new and cleaner synthesis. *Chem. Soc. Rev.* **2012**, *41*, 413.

[2] P. Baláž, M. Achimovicova, M. Baláž, P. Billik, Z. Cherkezova-Zheleva, J. M. Criado, F. Delogu, E. Dutkova, E. Gaffet, F. J. Gotor, R. Kumar, I. Mitov, T. Rojac, M. Senna, A. Streletskii, K. Wieczorek-Ciurowa, Hallmarks of mechanochemistry: from nanoparticles to technology. *Chem. Soc. Rev.* **2013**, *42,* 7571.

[3] V. Šepelák, A. Düvel, M. Wilkening, K. D. Becker, P. Heitjans, Mechanochemical reactions and syntheses of oxides. *Chem. Soc. Rev.* **2013**, *42,* 7507.

[4] F. Preishuber-Pflügl, M. Wilkening, Mechanochemically synthesized fluorides: local structures and ion transport. *Dalton. Trans.* **2016**, *45,* 8675.

[5] P. Heitjans, S. Indris, Diffusion and ionic conduction in nanocrystalline ceramics. *J. Phys.: Condens. Matter.* **2003**, *15,* R1257.

[6] S. Indris, D. Bork, P. Heitjans, Nanocrystalline oxide ceramics prepared by high-energy ball milling. *J. Mater. Synth. Process.* **2000**, *8,* 245.

[7] M. Wilkening, V. Epp, A. Feldhoff, P. Heitjans, Tuning the Li diffusivity of poor ionic conductors by mechanical treatment: high Li conductivity of strongly defective $LiTaO_3$ nanoparticles. *J. Phys. Chem. C* **2008**, *112,* 9291.

[8] P. Heitjans, E. Tobschall, M. Wilkening, Ion transport and diffusion in nanocrystalline and glassy ceramics. *Eur. Phys. J. – Spec. Top.* **2008**, *16,1* 97.

[9] V. Epp, M. Wilkening, Motion of Li^+ in nanoengineered $LiBH_4$ and $LiBH_4$:Al_2O_3 comparison with the microcrystalline form. *ChemPhysChem* **2013**, *14,* 3706.

[10] A. Düvel, J. Bednarcik, V. Šepelák, P. Heitjans, Mechanosynthesis of the fast fluoride ion conductor $Ba_{1-x}La_xF_{2+x}$: from the fluorite to the tysonite structure. *J. Phys. Chem. C* **2014**, *118,* 7117.

[11] G. Scholz, S. Breitfeld, T. Krahl, A. Düvel, P. Heitjans, E. Kemnitz, Mechanochemical synthesis of MgF_2 – MF_2 composite systems (M = Ca, Sr, Ba). *Solid State Sci.* **2015**, *50,* 32.

[12] S. Kipp, V. Šepelák, K. D. Becker, Mechanochemistry. *Chem. unserer Zeit* **2005**, *39,* 384.

[13] V. Šepelák, I. Bergmann, S. Kipp, K. D. Becker, Nanocrystalline ferrites prepared by mechanical activation and mechanosynthesis. *Z. Anorg. Allg. Chem.* **2005**, *631,* 993.

[14] A. Düvel, B. Ruprecht, P. Heitjans, M. Wilkening, Mixed alkaline-earth effect in the metastable anion conductor $Ba_{1-x}Ca_xF_2$ ($0 \le x \le 1$): correlating long-range ion transport with local structures revealed by ultrafast ^{19}F MAS NMR. *J. Phys. Chem. C* **2011**, *115,* 23784.

[15] B. Ruprecht, M. Wilkening, A. Feldhoff, S. Steuernagel, P. Heitjans, High anion conductivity in a ternary non-equilibrium phase of BaF_2 and CaF_2 with mixed cations. *Phys. Chem. Chem. Phys.* **2009**, *11,* 3071.

[16] B. Ruprecht, M. Wilkening, S. Steuernagel, P. Heitjans, Anion diffusivity in highly conductive nanocrystalline BaF_2:CaF_2 composites prepared by high-energy ball milling. *J. Mater. Chem.* **2008**, *18,* 5412.

[17] F. Preishuber-Pflügl, P. Bottke, V. Pregartner, B. Bitschnau, M. Wilkening, Correlated fluorine diffusion and ionic conduction in the nanocrystalline F^- solid electrolyte $Ba_{0.6}La_{0.4}F_{2.4}$ - ^{19}F $T_{1\rho}$ NMR relaxation vs. conductivity measurements. *Phys. Chem. Chem. Phys.* **2014**, *16,* 9580.

[18] F. Preishuber-Pflügl, V. Epp, S. Nakhal, M. Lerch, M. Wilkening, Defect-enhanced F^- ion conductivity in layer-structured nanocrystalline $BaSnF_4$ prepared by high-energy ball milling combined with soft annealing. *Phys. Status Solidi C* **2015**, *12,* 10.

[19] F. Preishuber-Pflügl, M. Wilkening, Evidence of low dimensional ion transport in mechanosynthesized nanocrystalline $BaMgF_4$. *Dalton. Trans.* **2014**, *43*, 9901.

[20] D. Wohlmuth, V. Epp, M. Wilkening, Fast Li ion dynamics in the solid electrolyte $Li_7P_3S_{11}$ as probed by ^{6,7}Li NMR spin-lattice relaxation. *ChemPhysChem* **2015**, *16*, 2582.

[21] C. Rongeat, M. A. Reddy, R. Witter, M. Fichtner, Nanostructured fluorite-type fluorides as electrolytes for fluoride ion batteries. *J. Phys. Chem. C* **2013**, *117*, 4943.

[22] C. Suryanarayana, Mechanical alloying and milling. *Prog. Mater Sci.* **2001**, *46,* 1.

[23] F. P. Bowden, D. Tabor, *The friction and lubrication of solids*, Clarendon Press, Oxford, **1958**.

[24] F. P. Bowden, A. Yoffe. *Initiation and growth of explosion in liquids and solids*, Cambridge University Press, Cambridge, **1952**.

[25] F. P. Bowden, A. Yoffe, *Fast reactions in solids*, Butterworths, London, **1958**.

[26] P. A. Thiessen, K. Meyer, G. Heinicke *Grundlagen der Tribochemie*; Akademie-Verlag, Berlin, **1967**.

[27] P. Baláž. *Mechanochemistry in nanoscience and minerals engineering*; Springer-Verlag, Berlin, **2008**.

[28] A. Chadwick, S. Savin, Structure and dynamics in nanoionic materials. *Solid State Ion*. **2006**, *177*, 3001.
[29] P. Heitjans, M. Masoud, A. Feldhoff, M. Wilkening, NMR and impedance studies of nanocrystalline and amorphous ion conductors: lithium niobate as a model system. *Faraday Discuss.* **2007**, *134*, 67.
[30] D. Wohlmuth, V. Epp, B. Stanje, A. M. Welsch, H. Behrens, M. Wilkening, High-energy mechanical treatment boosts ion transport in nanocrystalline $Li_2B_4O_7$. *J. Am. Ceram. Soc.* **2016**, *99*, 1687.
[31] H. Brandstätter, D. Wohlmuth, P. Bottke, V. Pregartner, M. Wilkening, Li ion dynamics in nanocrystalline and structurally disordered Li_2TiO_3. *Z. Phys. Chem.* **2015**, *229*, 1363.
[32] R. Malik, D. Burch, M. Bazant, G. Ceder, Particle size dependence of the ionic diffusivity. *Nano Lett.* **2010**, *10*, 4123.
[33] L. W. Ji, Z. Lin, M. Alcoutlabi, X. W. Zhang, Recent developments in nanostructured anode materials for rechargeable lithium-ion batteries. *Energy. Environ. Sci.* **2011**, *4*, 2682.
[34] C. Liu, F. Li, L. P. Ma, H. M. Cheng, Advanced materials for energy storage. *Adv. Mater.* **2010**, *22*, E28.
[35] M. Holzapfel, H. Buqa, L. J. Hardwick, M. Hahn, A. Würsig, W. Scheifele, P. Novák, R. Kötz, C. Veit, F. M. Petrat, Nano silicon for lithium-ion batteries. *Electrochim. Acta* **2006**, *52*, 973.
[36] A. Dunst, V. Epp, I. Hanzu, S. A. Freunberger, M. Wilkening, Short-range Li diffusion vs. long-range ionic conduction in nanocrystalline lithium peroxide Li_2O_2 - the discharge product in lithium-air batteries. *Energy. Environ. Sci.* **2014**, *7*, 2739.
[37] A. Dunst, M. Sternad, M. Wilkening, Overall conductivity and NCL-type relaxation behavior in nanocrystalline sodium peroxide Na_2O_2 – consequences for Na-oxygen batteries. *Mat. Sci. Engin. B* **2016**, *211*, 85.
[38] W. Puin, P. Heitjans, Frequency dependent ionic conductivity in nanocrystalline CaF_2 studied by impedance spectroscopy. *Nanostruct. Mater.* **1995**, *6*, 885.
[39] W. Puin, S. Rodewald, R. Ramlau, P. Heitjans, J. Maier, Local and overall ionic conductivity in nanocrystalline CaF_2. *Solid State Ion*. **2000**, *131*, 159.
[40] W. Puin, P. Heitjans, W. Dickenscheid, H. Gleiter. in *Defects in Insulating Materials*, (Eds. O. Kanert and J.-M. Spaeth) World Scientific, Singapore, p. 137, **1993**.
[41] P. Heitjans, A. Schirmer, S. Indris. in *Diffusion in Condensed Matter – Methods, Materials, Models*, (Eds. P. Heitjans and J. Kärger) Springer, Berlin, p. 367, **2005**.
[42] J. Maier, Ionic conduction in space charge regions. *Prog. Solid State Chem*. **1995**, *23*, 171.
[43] N. Sata, K. Eberman, K. Eberl, J. Maier, Mesoscopic fast ion conduction in nanometre-scale planar heterostructures. *Nature* **2000**, *408*, 946.
[44] J. Maier, Nanoionics: ion transport and electrochemical storage in confined systems. *Nat. Mater.* **2005**, *4*, 805.
[45] J. Maier, Nanoionics: ionic charge carriers in small systems. *Phys. Chem. Chem. Phys*. **2009**, *11*, 3011.
[46] J. Maier, Pushing nanoionics to the limits: charge carrier chemistry in extremely small systems. *Chem. Mater.* **2014**, *26*, 348.
[47] D. R. Figueroa, A. V. Chadwick, J. H. Strange, NMR relaxation, ionic conductivity and self-diffusion process in barium fluoride. *J. Phys. C Solid State* **1978**, *11*, 55.
[48] A. Düvel, M. Wilkening, R. Uecker, S. Wegner, V. Šepelák, P. Heitjans, Mechanosynthesized nanocrystalline $BaLiF_3$: the impact of grain boundaries and structural disorder on ionic transport. *Phys. Chem. Chem. Phys.* **2010**, *12*, 11251.
[49] S. Breuer, M. Wilkening: to be published **2016**.
[50] A. Kuhn, M. Kunze, P. Sreeraj, H. D. Wiemhöfer, V. Thangadurai, M. Wilkening, P. Heitjans, NMR relaxometry as a versatile tool to study Li ion dynamics in potential battery materials. Solid State Nucl. Magn. *Reson* **2012**, *42*, 2.
[51] A. Kuhn, S. Narayanan, L. Spencer, G. Goward, V. Thangadurai, M. Wilkening, Li self-diffusion in garnet-type $Li_7La_3Zr_2O_{12}$ as probed directly by diffusion-induced ^7Li spin-lattice relaxation NMR spectroscopy. *Phys. Rev. B* **2011**, *83*, 094302.
[52] D. Zahn, P. Heitjans, J. Maier, From composites to solid solutions: modeling of ionic conductivity in the CaF_2-BaF_2 system. *Chem. Eur. J.* **2012**, *18*, 6225.
[53] A. V. Chadwick, A. Düvel, P. Heitjans, D. M. Pickup, S. Ramos, D. C. Sayle, T. X. T. Sayle, X-ray absorption spectroscopy and computer modelling study of nanocrystalline binary alkaline earth fluorides. Inst. Phys.: Conf. Series: *Mat. Sci. Engin.* **2015**, *80*, Article no: 012005, 4 pages.
[54] A. Düvel, S. Wegner, K. Efimov, A. Feldhoff, P. Heitjans, M. Wilkening, Access to metastable complex ion conductors via mechanosynthesis: preparation, microstructure and conductivity of (Ba,Sr)LiF_3 with inverse perovskite structure. *J. Mater. Chem.* **2011**, *21*, 6238.
[55] L. N. Patro, K. Hariharan, Fast fluoride ion conducting materials in solid state ionics: an overview. *Solid State Ion*. **2013**, *239*, 41.
[56] F. Gingl, $BaMgF_4$ and $Ba_2Mg_3F_{10}$: new examples for structural relationships between hydrides and fluorides. Z. *Anorg. Allg. Chem.* **1997**, *623*, 705.
[57] C. V. Kannan, K. Shimamura, H. R. Zeng, H. Kimura, E. G. Villora, K. Kitamura, Ferroelectric and anisotropic electrical properties of $BaMgF_4$ single crystal for vacuum UV devices. *J. Appl. Phys.* **2008**, *104*, 114113.
[58] D. L. Sidebottom, Dimensionality dependence of the conductivity dispersion in ionic materials. *Phys. Rev. Lett.* **1999**, *83*, 983.
[59] S. W. Kim, H. Y. Chang, P. S. Halasyamani, selective pure-phase synthesis of the multiferroic $BaMF_4$ (M = Mg, Mn, Co, Ni, and Zn) family. *J. Am. Chem. Soc.* **2010**, *132*, 17684.
[60] R. M. Kowalczyk, T. F. Kemp, D. Walker, K. J. Pike, P. A. Thomas, J. Kreisel, R. Dupree, M. E. Newton, J. V. Hanna, M. E. Smith, A variable temperature solid-state nuclear magnetic resonance, electron paramagnetic resonance and Raman scattering study of molecular dynamics in ferroelectric fluorides. *J. Phys.: Condes. Matter.* **2011**, *23*, Article no: 315402, 16 pages.
[61] F. Preishuber-Pflügl, M. Wilkening: to be published **2016**.
[62] S. Chaudhuri, F. Wang, C. P. Grey, Resolving the different dynamics of the fluorine sublattices in the anionic conductor $BaSnF_4$ by using high-resolution MAS NMR techniques. *J. Am. Chem. Soc.* **2002**, *124*, 11746.
[63] G. Dénès, T. Birchall, M. Sayer, M. F. Bell, $BaSnF_4$ – a new fluoride ionic conductor with the α-$PbSnF_4$ structure. *Solid State Ion.* **1984**, *13*, 213.
[64] G. Dénès, J. Hantash, A. Muntasar, P. Oldfield, A. Bartlett, Variations of $BaSnF_4$ fast ion conductor with the method of preparation and temperature. *Hyperfine Interact* **2007**, *170*, 145.
[65] L. N. Patro, K. Hariharan, Influence of synthesis methodology on the ionic transport properties of $BaSnF_4$. *Mater. Res. Bull.* **2011**, *46*, 732.
[66] J.-M Réau, C. Lucat, J. Portier, P. Hagenmuller, L. Cot, S. Vilminot, Etude des proprietes structurales et electrioues d'un nouveau conducteur anionique: $PbSnF_4$. *Mater. Res. Bull.* **1978**, *13*, 877.

[67] A. V. Chadwick, E.-S. Hammam, D. van der Putten, J. H. Strange, Studies of ionic transport in MF_2-SnF_2 systems. *Cryst. Latt. Def. Amorph. Mat.* **1987**, *15*, 303.

[68] V. Šepelák, S. M. Becker, I. Bergmann, S. Indris, M. Scheuermann, A. Feldhoff, C. Kübel, M. Bruns, N. Stürzl, A. S. Ulrich, M. Ghafari, H. Hahn, C. P. Grey, K. D. Becker, P. Heitjans, Nonequilibrium structure of Zn_2SnO_4 spinel nanoparticles. *J. Mater. Chem.* **2012**, *22*, 3117.

[69] V. Šepelák, M. Myndyk, M. Fabián, K. L. Da Silva, A. Feldhoff, D. Menzel, M. Ghafari, H. Hahn, P. Heitjans, K. D. Becker, Mechanosynthesis of nanocrystalline fayalite Fe_2SiO_4. *Chem. Commun. (Camb)* **2012**, *48*, 11121.

[70] V. Šepelák, S. Begin-Colin, G. Le Caer, Transformations in oxides induced by high-energy ball-milling. *Dalton. Trans.* **2012**, *41*, 11927.

[71] K. L. Da Silva, D. Menzel, A. Feldhoff, C. Kübel, M. Bruns, A. Paesano, A. Düvel, M. Wilkening, M. Ghafari, H. Hahn, F. J. Litterst, P. Heitjans, K. D. Becker, V. Šepelák, Mechanosynthesized $BiFeO_3$ nanoparticles with highly reactive surface and enhanced magnetization. *J. Phys. Chem. C* **2011**, *115*, 7209.

[72] V. Šepelák, M. Myndyk, R. Witte, J. Roder, D. Menzel, R. H. Schuster, H. Hahn, P. Heitjans, K. D. Becker, The mechanically induced structural disorder in barium hexaferrite $BaFe_{12}O_{19}$ and its impact on magnetism. *Faraday Discuss.* **2014**, *170*, 121.

[73] A. Düvel, E. Romanova, M. Sharifi, D. Freude, M. Wark, P. Heitjans, M. Wilkening, Mechanically induced phase transformation of γ-Al_2O_3 into α-Al_2O_3: access to structurally disordered γ-Al_2O_3 with a controllable amount of pentacoordinated Al sites. *J. Phys. Chem. C* **2011**, *115*, 22770.

[74] V. Šepelák, I. Bergmann, S. Indris, A. Feldhoff, H. Hahn, K. D. Becker, C. P. Grey, P. Heitjans, High-resolution ^{27}Al MAS NMR spectroscopic studies of the response of spinel aluminates to mechanical action. *J. Mater. Chem.* **2011**, *21*, 8332.

[75] M. Fabián, P. Bottke, V. Girman, A. Düvel, K. L. Da Silva, M. Wilkening, H. Hahn, P. Heitjans, V. Šepelák, A simple and straightforward mechanochemical synthesis of the far-from-equilibrium zinc aluminate, $ZnAl_2O_4$, and its response to thermal treatment. *RSC Adv.* **2015**, *5*, 54321.

[76] L. J. Berchmans, M. Myndyk, K. L. Da Silva, A. Feldhoff, J. Šubrt, P. Heitjans, K. D. Becker, V. Šepelák, A rapid one-step mechanosynthesis and characterization of nanocrystalline $CaFe_2O_4$ with orthorhombic structure. *J. Alloys Compd.* **2010**, *500*, 68.

[77] V. Šepelák, K. D. Becker, I. Bergmann, S. Suzuki, S. Indris, A. Feldhoff, P. Heitjans, C. P. Grey, A one-step mechanochemical route to core-shell Ca_2SnO_4 nanoparticles followed by ^{119}Sn MAS NMR and ^{119}Sn Mössbauer spectroscopy. *Chem. Mater.* **2009**, *21*, 2518.

[78] J. H. Kwak, J. Z. Hu, D. Mei, C. W. Yi, D. H. Kim, C. H. F. Peden, L. F. Allard, J. Szanyi, Coordinatively unsaturated Al^{3+} centers as binding sites for active catalyst phases of Platinum on γ-Al_2O_3. *Science* **2009**, *325*, 1670.

[79] D. H. Mei, J. H. Kwak, J. Z. Hu, S. J. Cho, J. Szanyi, L. F. Allard, C. H. F. Peden, Unique role of anchoring penta-coordinated Al^{3+} sites in the sintering of γ-Al_2O_3-Supported Pt catalysts. *J. Phys. Chem. Lett.* **2010**, *1*, 2688.

[80] S. K. Lee, S. Y. Park, Y. S. Yi, J. Moon. Structure and disorder in amorphous alumina thin films: Insights from high-resolution solid-state NMR. *J. Phys. Chem. C* **2010**, *114*, 13890.

[81] A. Qiao, V. N. Kalevaru, J. Radnik, A. Düvel, P. Heitjans, A. S. H. Kumar, P. S. S. Prasad, N. Lingaiah, A. Martin, Oxidative dehydrogenation of ethane to ethylene over V_2O_5/Al_2O_3 catalysts: effect of source of alumina on the catalytic performance. *Ind. Eng. Chem. Res.* **2014**, *53*, 18711.

[82] J. H. Kwak, J. Z. Hu, D. H. Kim, J. Szanyi, C. H. F. Peden, Penta-coordinated Al^{3+} ions as preferential nucleation sites for BaO on γ-Al2O_3: An ultra-high-magnetic field ^{27}Al MAS NMR study. *J. Catal.* **2007**, *251*, 189.

[83] J. H. Kwak, J. Z. Hu, A. Lukaski, D. H. Kim, J. Szanyi, C. H. F. Peden, Role of pentacoordinated Al^{3+} ions in the high temperature phase transformation of γ-Al_2O_3. *J. Phys. Chem. C* **2008**, *112*, 9486.